Phosphorylation, disorder, and phase separation govern the behavior of Frequency in the fungal circadian clock

Daniyal Tariq[a,*], Nicole Maurici[b,*], Bradley M. Bartholomai[c], Siddarth Chandrasekaran[a], Jay C. Dunlap[c], Alaji Bah[b,1] and Brian R. Crane[a,1].

[a]Department of Chemistry & Chemical Biology, Cornell University, Ithaca, NY,14853;

[b]Department of Biochemistry and Molecular Biology, SUNY Upstate Medical University, Syracuse, NY, 13210;

[c]Department of Molecular and Systems Biology, Geisel School of Medicine at Dartmouth, Hanover, NH 03755

*Denotes equal contribution

[1]To whom correspondence may be addressed. BahA@upstate.edu; bc69@cornell.edu.

Abstract

Circadian clocks are composed from molecular oscillators that pace rhythms of gene expression to the diurnal cycle. Therein, transcriptional-translational negative feedback loops (TTFLs) generate oscillating levels of transcriptional repressor proteins that regulate their own gene expression. In the filamentous fungus *Neurospora crassa,* the proteins **F**requency (**F**RQ), the **F**RQ-interacting RNA helicase (FRH) and **C**asein-Kinase I (CK1) form the **FFC** complex that acts to repress expression of clock-controlled genes activated by the White-Collar complex (WCC). A key question concerns how the FRQ protein orchestrates molecular interactions at the core of the clock despite containing little tertiary structure. We present the reconstitution and biophysical characterization of FRQ and the FFC complex in unphosphorylated and highly phosphorylated states. An integrated structural and computational biology approach incorporating site-specific spin labeling and pulse-dipolar ESR spectroscopy provides domain-specific structural details on FRQ and the FFC. FRQ, although substantially disordered, contains a compact core that associates and organizes FRH and CK1 to coordinate their roles in WCC repression. Phosphorylation of FRQ increases conformational flexibility and alters oligomeric state but the resulting changes in structure and dynamics are non-uniform. FRQ undergoes liquid-liquid phase separation (LLPS) in a phosphorylation dependent manner to sequester FRH and CK1 and influence CK1 enzymatic activity. Live imaging of *Neurospora* hyphae reveals FRQ foci near the nuclear periphery characteristic of condensates. Analog clock repressor proteins in higher

organisms share little position-specific sequence identity with FRQ; yet, they contain amino-acid compositions that promote LLPS. Hence, condensate formation may be a conserved feature of eukaryotic circadian clocks.

Significance

The central transcriptional repressor proteins of circadian clocks are often highly disordered, undergo extensive post-translational modification and have poorly defined structural properties. The fungal repressor protein Frequency (FRQ) nucleates a semi-ordered molecular assembly that despite conformational heterogeneity arranges its components in close proximity and facilitates their sequestration and enzymatic regulation through post-translational modification and liquid-liquid phase separation. Analogous properties are predicted by the similar amino acid compositions of clock proteins in insects and mammals.

Introduction

Eukaryotic circadian rhythms of biological phenomena arise from periodic gene expression patterns that oscillate independent of external cues but can be entrained to light and temperature (1). At the molecular level, circadian clocks function as transcription-translation negative-feedback loops (TFFLs) that consist of core positive and negative elements (Fig. 1A (2)). In the long-standing model clock of *Neurospora crassa*, the negative transcriptional repressor complex is known as the FFC: named for its three principal components: Frequency (FRQ, Fig. 1B), the FRQ-interacting RNA helicase (FRH) and Casein Kinase 1 (CK1) (1, 3). FRQ is functionally analogous to Period (PER) in insects and mammals, whereas CK1 is an ortholog of the mammalian CK1 and the Drosophila kinase Doubletime (DBT) (4). FRH is found only in the core repressor of the fungal clock. Although FRH is homologous to the yeast helicase MTR4, FRH helicase activity does not appear essential to clock function (5, 6). The FFC represses the positive arm of the cycle, which involves two zinc-finger transcription factors, White-Collar 1 (WC-1) and White-Collar 2 (WC-2) assembled into the White-Collar Complex (WCC).

WCC binding to the clock-box (c-box) activates *frq* expression (Fig. 1A (7)). FRQ production is also highly regulated at the post-transcriptional level through the use of rare codons to retard translation, the expression of an anti-sense transcript and alternative splicing mechanisms (3, 4, 8). The latter leads to the production of either a long (L-FRQ) or short (S-FRQ) isoform, and the

2

ratio of these isoforms fine tunes period length in response to ambient temperatures (8-10). Translated FRQ binds to FRH via its FFD domain and CK1 via its two FCD domains (1 and 2) to form the repressive FFC (Fig. 1C). The FFC enters the nucleus where it directly inhibits the WCC and thereby down-regulates *frq* expression (11). FRQ-mediated WCC phosphorylation by CK1 (and associated kinases) reduces interactions between the WCC and the c-box to close the feedback loop and restart the cycle (Fig. 1A (12)). FRH facilitates interactions between the FFC and the WCC (6) and thus, repressor function likely depends upon the FRQ-mediated association of CK1 and FRH. Whereas interaction regions on the FRQ protein sequence have been identified (Fig. 1C), there is little information on the spatial arrangement of the FFC components.

Despite low sequence conservation among the core negative arm proteins across species, they all share a high degree of disorder (13). FRQ, the analogous Drosophila (d) Period (PER) protein and the analogous mammalian (m) PER have > 65% disorder predicted in their sequences with ~86% of the FRQ sequence assumed to have no defined structure (13). Both FRQ and mPER2 have biochemical properties characteristic of intrinsically disordered proteins (IDPs) (5, 11). These clock repressors also undergo extensive posttranslational modification (PTM), particularly phosphorylation (13, 14). FRQ acquires over 100 phosphorylation sites over the course of the circadian day (similar to PER phosphorylation by DBT), predominantly due to CK1 (15). The phosphorylation events have two consequences: 1) those that weaken the interaction between FRQ and the WCC or CK1 (3, 16); and 2) those that direct FRQ down the ubiquitin-proteasome pathway (17), although only the former are required for circadian rhythmicity (17). Multi-site phosphorylation of FRQ influences its inhibitory function and clock period length (16, 17); several studies have reported variable trypsin sensitivities of the different phospho-forms (13, 16). Although the consequences of phosphorylation-driven conformational changes in FRQ have been thus probed, the challenges of producing FRQ have limited direct assessment of its conformational properties (13, 16, 18). IDPs such as FRQ are known to participate in liquid-liquid phase separation (LLPS), which has emerged as a key mechanism for organizing cellular components, coordinating metabolism and directing signaling through, for example, the formation of membraneless organelles (MLOs) (18, 19). Emerging studies in plants (20) and flies (21) implicate LLPS in circadian clocks and in *Neurospora* it has recently been shown that the Period-2 (PRD-2) RNA-binding protein influences *frq* mRNA localization through a mechanism potentially mediated by LLPS (22). Intriguing questions surround why clock repressor proteins are so disordered, undergo extensive post-translational modification and whether LLPS has a role to play in their function.

Clock proteins and their complexes have been challenging to characterize due to their large size (>100 kDa), low sequence complexity, extensive disorder and modification states. Herein, we reconstitute FRQ and the FFC to assess the global and site-specific structural properties of these moieties, as well as the dependence of their properties on multi-site phosphorylation. FRQ undergoes non-uniform conformational change upon phosphorylation and arranges FRH close to CK1 in the FFC. We also demonstrate that FRQ indeed participates in phosphorylation-dependent LLPS, and as a condensate sequesters FRH and CK1 while altering CK1 activity. Our results show how a massively disordered protein such as FRQ organizes the clock core oscillator and reveal the effects of extensive phosphorylation on the conformational and phase-separation properties of a large IDP.

Results:

Sequence assessment and general properties of FRQ

Analysis of an AlphaFold 2.0 (23) model of full-length FRQ indicates that FRQ lacks a defined arrangement of large folded domains; instead, most of the molecule is unstructured (Fig. 1B), in agreement with previous studies predicting that FRQ mostly comprises intrinsically disordered regions (5). However, FRQ is also predicted to contain a small, clustered core, with several secondary structural elements that collapse together to form a compact nucleus surrounded by long flexible disordered regions (Fig. 1B). The AlphaFold pLDDT scores, which represent the confidence in the structural prediction (23), are very low across the model, except within the core (cyan, *SI Appendix*, Fig. S1), which contains the CK1 binding region. The FRH binding region falls within a more flexible region with a lower pLDDT score than that of CK1. Helices compose the majority of secondary structural elements predicted by AlphaFold (Fig. 1B). These assignments were generally supported by the Agadir program that predicts helical propensity based on the helix/coil transition theory (24). Four regions distributed throughout the length of FRQ (residues 194-212, 312-329, 709-719 and 801-817) have at least 10% helical propensity and these helical regions mostly agree with those of the AlphaFold model (Fig. 1B). Together, these sequence analyses suggest that FRQ assumes a broad conformational ensemble containing an ordered nucleus that interacts extensively with partially ordered and flexible regions.

Reconstitution of FRQ in unphosphorylated and highly phosphorylated states

4

The size and intrinsic disorder of FRQ have made it challenging to recombinantly express and purify. Previous purifications have characterized FRQ as an IDP, but suffered from low yields and aggregated species (11, 25).   We also encountered extensive protein degradation and aggregation with conventional purification methods and affinity tagging strategies; however, methods proven effective for IDPs (26) yielded comparatively well-behaved protein. Briefly, we carried out Nickel affinity chromatography and size exclusion chromatography (SEC) under denaturing conditions to maximize yield and reduce aggregation of full-length L-FRQ (residues 1-989; Fig. 2A) (27). Solubilization with high concentrations of guanidinium-HCl prevented proteolysis, aggregation and limited co-purification of impurities that were otherwise difficult to remove. Once FRQ was isolated, the protein remained soluble, monodisperse and could be concentrated after the denaturant was removed by dialysis (Fig. 2A,B). To our knowledge, FRQ is one of the largest native IDPs produced in amounts amenable to structural and biophysical characterization.

To generate phosphorylated FRQ, the protein was co-expressed with CK1, which forms a stable complex with FRQ and acts as its primary kinase (28). Phosphorylation was confirmed visually by SDS-PAGE (Fig. 2B) and mass spectrometry (*SI* Appendix, Fig. S2). The latter revealed a network of > 80 phosphorylation sites (*SI* Appendix, Fig. S2), most of which agree with those found on natively expressed FRQ (15, 29). Hereafter, we refer to this preparation as phosphorylated FRQ (p-FRQ) whereas non-phosphorylated FRQ (np-FRQ) refers to FRQ expressed without CK1. In general, we found that co-expression of FRQ with CK1 increased protein yield and stability, while limiting aggregation and degradation.

Global properties of FRQ

Size Exclusion Chromatography coupled to Multi Angle Light Scattering (SEC-MALS) of p-FRQ gives a molecular weight measurement consistent with a primarily monomeric state (MW of ~143 kDa versus a predicted MW of ~110 kDa; Fig. 2B). In contrast, the np-FRQ measured by MALS indicates a dimer and its measured mass distribution increases upon concentration (Fig. 2B) Hence, purified np-FRQ dimerizes, whereas phosphorylation destabilizes this association. SEC-coupled small-angle x-ray scattering (SAXS) analyses revealed that both p-FRQ and np-FRQ shared characteristics of highly flexible proteins, but that p-FRQ was more extended than np-FRQ (*SI Appendix* Table S1). The dimensionless Kratky plots of p-FRQ and np-FRQ, which report on compactness and conformational dispersity (30-33), revealed high degrees of flexibility for both proteins (Fig. 2C). The peak values of the plot were shifted from those expected for compact

structures but were also not indicative of fully disordered proteins (32, 34, 35). Furthermore, p-FRQ appears more disordered than np-FRQ; a characteristic also reflected in their pairwise distance distributions (*SI Appendix*, Fig. S3). These data then indicate that FRQ generally adopts a relatively monodisperse conformational state that is partially compact but highly flexible and increases overall extent upon phosphorylation.

Local measures of FRQ structure and dynamics

The properties of FRQ that include its intrinsic disorder and propensity to form heterogenous ensembles are not well suited to commonly applied structural characterization methods. We applied site-specific spin labeling (Fig. 3A) and electron spin resonance spectroscopy (ESR) to monitor FRQ local structural properties. FRQ has four native cysteine residues that provide reactive sites for nitroxide spin-labels (Fig. 3A,B (36)). The Cys residues distribute relatively evenly throughout the protein sequence and fall within areas of varying structural order that include the binding regions for the core clock proteins (FRH, CK1, WC1 and WC2; *SI Appendix*, Table S2-3; Fig. 3B). Furthermore, we developed and applied enzymatic SortaseA & AEP1 peptide-coupling methods (37, 38) to spin-label FRQ at its N- and C- termini (Fig. 3A; *SI Appendix* Fig. S4).

Line-shape analysis from continuous wave (cw)-ESR spectroscopy reports on local dynamics (39, 40). For rapidly rotating nitroxide spin labels (SLs), the characteristic spectrum consists of three narrow lines of equal width and intensity. As the rotational mobility decreases, the lines broaden, especially the high-field line (41, 42). Cw-ESR reveals that FRQ has regions of varying order that agree with computational predictions and that some of these sites undergo phosphorylation-dependent conformational changes (Fig. 3C). Spin-labels attached to Cys490 and Cys658 (490SL and 658SL) are predicted to be within an α-helix and a β-strand respectively. These sites correspondingly showed a broad low-field (left-most line) component and a small high-field component (right-most line) indicative of slower tumbling compared to sites predicted to be in flexible regions, such as 746SL (Fig. 3C). The 490SL site had a broader profile compared to that of the 658SL site, although both are relatively well ordered. We observed a similar trend with δ, which is the peak-to-peak width of the central line (43). 490SL and 658SL had similar δ values that were higher than that of 746SL, indicating that they are less flexible than 746SL (*SI Appendix* Table S4). Furthermore, the spectra also highlighted structural differences between the phospho forms: p-FRQ and np-FRQ gave very different δ values at 490SL and the C-terminus, thereby

6

demonstrating how phosphorylation can influence conformational properties site-specifically. The C-terminus may have become more dynamic in p-FRQ as compared to np-FRQ because the C-terminus contains a cluster of phospho-sites (Fig. 3C). In contrast, the N-terminus and especially 490SL, which locates to the CK1-interaction region of the FCD domain, are more ordered in p-FRQ. Such differences in mobility between p-FRQ and np-FRQ in the FCD (490SL) may reflect changes in FRQ:CK1 interactions as FRQ becomes progressively phosphorylated across the circadian period (16).

Double electron–electron resonance (DEER) spectroscopy provides distance distribution between two nitroxide labels in the range of 15 Å to ~100 Å. We produced 6 cysteine pair variants that each contained only two of the four native FRQ Cys residues to measure pair-wise distances and one single Cys variant to test for oligomerization. Owing to association and aggregation when concentrated, np-FRQ was not amenable to DEER measurements; however, such issues were not prohibitive with p-FRQ. Consistent with the MALS data showing p-FRQ to be monomeric, the single Cys spin-labeled variant 490SL produced very little dipolar signal that would otherwise indicate dimerization. Likewise, the double 370SL:746SL p-FRQ variant also gave no dipolar signals and hence no dimerization as reported by those two sites (Fig. 3D). The DEER experiments of the Cys pairs generally revealed slow decaying time domain traces when at least one of the two cysteine residues resides outside of the predicted core (Fig. 3D; *SI Appendix* Fig. S5-6). Such traces are indicative of long inter-spin distances and conformational flexibility, which would be consistent with the large mobility and intrinsic disorder of these peripheral regions (*SI Appendix*, Fig. S5). Only variant 490SL:658SL, wherein both labeling sites fall within the ordered core, gave a fast-decaying time-domain signal, indicative of short inter-spin distances and conformational rigidity (*SI Appendix*, Fig. S5-6).

FFC reconstitution and component arrangement.

The FFC was generated by mixing p-FRQ or np-FRQ with excess FRH and CK1 followed by SEC purification to give p-FFC or np-FFC, respectively. FRHΔN (residues 100-1106), which binds FRQ, was used to improve expression and enhance stability (6, 11). The resulting symmetric SEC traces and SDS-PAGE gels revealed pure and homogenous ternary complexes in each case (Fig. 4A). As expected, CK1 phosphorylates FRQ in np-FFC (Fig. 4A, *SI Appendix* Fig. S7) and this activity does not require priming by other kinases (44). SEC-SAXS analysis of the FFC showed that both FRQ phosphor-forms produced complexes that were more globular than FRQ alone, but still somewhat flexible, with the p-FFC more dynamic than the np-FFC (Fig. 4B, *SI Appendix*,

7

Fig. S3). MW estimates of the p-FFC and np-FFC from SAXS indicate a 1:1 stoichiometry of FRQ:FRH, with a likely single component of CK1 also contained within the complex (Table S1).

DEER measurements from selectively spin-labeled components within the complex were used to probe its overall architecture (Fig. 5; *SI Appendix* Fig. S8-S11). An ADP-βSL probe (45) bound to both FRH and CK1 and revealed that the FRH and CK1 ATP-binding pockets are closely positioned within the FFC complex (Fig. 5A; Fig. *SI Appendix* S8). Nonetheless, the presence of broad and multiple peaks in the distance distributions indicated conformational heterogeneity. Spin labels placed within the FCD2 and FFD domains of FRQ (490C and 746C), which bind CK1 and FRH respectively, produced a distance distribution similar to that of the labels that target the ATP binding sites of the two enzymes (Fig. 5A) (46).

Spin-label separations within p-FRQ changed substantially when FRH and CK1 bound (Fig. 5; *SI Appendix* Fig. S9-S11). In general, the resulting distance distributions had smaller mean distances and less breadth (Fig. 5B-G). However, the changes were not uniform; for example, the 658SL-to-746SL distance increased in the complex compared to free FRQ (Fig. 5G). To assess how the populations of the two major classes of p-FRQ conformations changed when the p-FFC formed, the distance data was fit to a two-state Gaussian model (*SI Appendix*, Fig. S12; *SI Appendix* Table S5). Population changes were most prominent for the 370-658, 490-658 and 490-746 variants, which contain sites involved in core clock interactions (Fig. 5H). The proportion of the more ordered conformation increased from ~30% to ~70% in the 370-658 variant (Fig. 5D) and from ~10% to ~70% in the 490-746 variant (Fig. 5F) when bound to FRH and CK1.The 490, 658 and 746 sites reside in regions important for WCC interactions (47) and FRH may organize such binding determinants. Notably, the 370SL:746SL spin pair showed little dipolar coupling in free p-FRQ but resolved into an observable mid-range separation in the presence of CK1 and FRH (Fig. 5C), perhaps because position 746 is within the FRH binding region. Thus, CK1 and FRH order p-FRQ to an appreciable degree and the two enzymes are adjacently positioned within the conformationally heterogeneous complex.

FRQ undergoes LLPS *in vitro* and *in vivo*

The unstructured regions and multivalent interactions of IDPs can lead to liquid-liquid phase separation (LLPS). Such de-mixing often manifests in the formation of biomolecular condensates within cells (48). As has been previously noted (13), FRQ may be capable of LLPS owing to its extensive disorder. We found that FRQ has a high propensity to undergo LLPS based on a set of

8

computational tools that evaluate charge distribution and clustering, long-range aromatic and non-aromatic π:π contacts and nucleic acid binding propensies (49, 50). The overall FRQ PScore, which grades LLPS propensity on these properties (50), was 6.39, with three regions scoring above a value of 2, the threshold for favorable LLPS (*SI Appendix*, Fig. S13). The region with the highest PScore also accounted for the majority of LLPS propensity as determined by the catGRANULE prediction algorithm (49). Furthermore, we found that these methods also predicted the functional analogs dPER and hPER1 to phase-separate (Fig. 6A, *SI Appendix*, Fig. S14) The FRQ functional analogs share physicochemical characteristics with FRQ, particularly an enrichment of hydrophilic residues, increases in Gly and Pro content and a depletion of hydrophobic residues, even though their positional sequence conservation with FRQ is low (*SI Appendix*, Fig. S15 and S16). Similar amino acid composition patterns among FRQ, dPER and hPER1, include the most common residues in each protein and its UniRef50 cluster (sequences with at least 50% identity with the target protein) being serine, proline and glycine (~30% of total sequence) accompanied by a high depletion in aromatic residues (only ~7.5%) (*SI Appendix*, Fig. S16). In addition, all of the sequences have a reduced proportion of hydrophobic residues such as A, I, L, and V and a slightly acidic isoelectric point. Thus, FRQ, dPER and hPER1 all have low overall hydropathy (*SI Appendix*, Fig. S15). However, in addition, FRQ and its homologs are unusual in their high Arg and Asp content, which tend to separate in charge blocks throughout their sequences (as indicated by high kappa values, *SI Appendix*, Fig. S15). Such charge clustering correlates with LLPS (51). Overall, this analysis suggests that like intrinsic disorder, LLPS driven by the physiochemical properties of the constituent residues, may be a conserved feature in the negative arm of the circadian clock.

We tested experimentally whether both np-FRQ and p-FRQ can undergo LLPS *in vitro.* UV-Vis turbidity assays as a function of temperature revealed that FRQ undergoes a low critical solution temperature (LCST) phase transition that is concentration and phosphorylation status-dependent. (Fig. 6B). Furthermore, upon exchanging concentrated samples of each FRQ phospho-form into a non-denaturing phase separation buffer, we observed the appearance of a turbid solution that contained microscopic droplets (Fig. 6C). The LLPS droplets dissolved at low temperature, and only formed at some specific higher temperatures for a given solution condition. In this case, high salt conditions (500 mM KCl) enhanced the LCST behavior for all protein concentrations tested (Fig. 6C) (52). Whereas this KCl concentration is non-physiological *per se*, the ionic strength conditions and effective solute concentrations in cells are comparatively high (53). Phosphorylation of FRQ substantially enhanced its ability to phase separate, mostly likely by

increasing the relative negative charges, altering the charge patterns, and providing more sites for multivalent interactions within the molecule (*SI Appendix*, Fig. S17)(51, 54).

Live cell imaging of *Neurospora crassa* expressing FRQ tagged with the fluorescent protein mNeonGreen at its C-terminus (FRQ[mNeonGreen]) revealed heterogeneous patterning of FRQ in nuclei (Fig. 6D). Bright foci were observed near the nuclear periphery, which is delineated by the cytoplasm facing nucleoporin Son-1 tagged with mApple at its C-terminus (Fig. 6D). Such foci are indicative of biomolecular condensate formation, which is characteristic of phase-separated IDPs (22, 55-57) and similar to that seen for clock proteins in *Drosophila* nuclei (21).

<u>Phase-separated FRQ recruits FRH and CK1 and alters CK1 activity</u>
The PScore and catGRANULE LLPS predictors gave low overall scores for the FRQ partners, FRH and CK1 (*SI Appendix*, Fig. S14). Nonetheless, FRH and CK1 may still act as clients that localize to the FRQ-formed LLPS droplets. Indeed, fluorescently-labeled FRH and CK1 were recruited into phase-separated FRQ droplets (Fig. 7A), but a control protein labeled with the same fluorophore, *E. coli* CheY, was not (*SI Appendix*, Fig. S18). The ability of FRQ to recruit its partner proteins into phase-separated droplets provides a means to sequester them and potentially control their availabilities and activities.

LLPS has been suggested to modulate the activities of enzymes by creating a microenvironment to alter substrate-sequestration and product-release (52). We tested the effect of FRQ LLPS on its phosphorylation by CK1, a key reaction for regulating the period of the clock (16). We compared the phosphorylation of FRQ by CK1 in phase separation buffer under different temperatures, using the latter as a proxy for degree of LLPS. CK1 autophosphorylation served as an internal control and its temperature dependence was consistent with previous studies that show increased catalytic activity at higher temperatures (44). As temperature increases drove more LLPS, the phosphorylation of FRQ decreased, even as CK1 autophosphorylation increased (Fig. 7B; *SI Appendix* Fig. S19). Quantitatively, we observed a reduction in FRQ phosphorylation by two-fold under LLPS conditions relative to conditions under which it does not phase-separate (Fig. 7B). Through application of cw-ESR we probed FRQ dynamics within the condensates. We observed a striking rigidification of spin labeled FRQ after LLPS (Fig. 7C). The reduction of CK1-mediated FRQ phosphorylation, which likely requires substantial dynamics given the distribution of phosphorylation sites throughout the FRQ sequence, may reflect this change in molecular dynamics. Thus, in addition to affecting the localization of FRQ and its partners, LLPS also

impacts the enzymatic activity of the complex, by perhaps modulating molecular encounters and motions essential for large scale phosphorylation.

Discussion

Within the TTFLs that define eukaryotic circadian clocks, large repressor proteins like FRQ compose cellular timing mechanisms by coordinating transient protein-protein interactions, nuclear entry, targeted protein degradation, and transcriptional repression (13). They compose dynamic macromolecular assemblies that achieve specificity in their functions despite assuming highly variable structures (13). As anticipated from its sequence (5, 13), FRQ is indeed a highly dynamic protein, but even in isolation, it is not completely disordered. The SAXS and ESR data indicate that FRQ has compact features that localize to an ordered core interspersed with dynamic regions. Notably the SAXS and DEER data suggest a degree of disorder that is substantially greater than that expected of a molten globule (58), but far from that of a completely denatured protein (33, 59). Although FRQ lacks the well-defined PAS domains of the analogous PER proteins (13), it also maintains a structured nucleus to anchor its more dynamic elements. The regions that bind CK1 and FRQ are the most ordered and they organize the two partners beside each other, in fact, they are in remarkably close proximity, as judged by spin-labels in their ATP binding pockets or in their binding domains. FRH mediates contacts to the WCC (6), whereas CK1 phosphorylates the WCC to close the TTFL (3, 12, 16, 17); hence, CK1 targeting to the WCC likely depends on FRQ associating FRH with CK1 (12).

Proteolytic sensitivity assays have suggested that increased phosphorylation across the day transitions FRQ from a "closed" to a more "open" state (13, 16, 28). The SAXS data reveal that p-FRQ and p-FFC are more expansive and show greater flexibility than do np-FRQ and np-FFC, respectively. Furthermore, np-FRQ has a greater tendency to self-associate. In the cell, completely unphosphorylated FRQ is likely short-lived, if present at all (15). Phosphorylation may stabilize FRQ against aggregation, yet also provides for enough conformational heterogeneity to poise FRQ near a degradation threshold (17). This idea is supported by the cw-ESR data (Fig. 3), which shows that phosphorylation causes some regions to increase and others to decrease in flexibility. The DEER data also demonstrates that binding to FRH and CK1 increases compactness of p-FRQ, particularly in the central-core that is responsible for binding the partners. In contrast, the FRQ C-terminus gains considerably flexibility in the FFC. FRQ has been suggested to assume a dimeric state because of a predicted coiled-coil region and formation of mixed dimers formed in cellular pull-down assays with differentially tagged FRQ subunits (60).

11

Np-FRQ does indeed dimerize when isolated; whereas p-FRQ is primarily monomeric alone. Furthermore, SAXS data indicates there is one copy of FRQ in both the reconstituted np-FFC and p-FFC. Hence phosphorylation has the potential to regulate the FRQ oligomeric state, which may in turn be linked to FFC assembly. Despite being a monomer in isolation, the pull-down data (60) indicates that association of p-FRQ may be mediated by other cellular factors, including LLPS.

FRQ has physicochemical features embedded within its sequence that give rise to LLPS and the FRQ clock analogs exhibit similar characteristics (*SI Appendix*, Fig. S15 and S16) FRQ and negative-arm proteins in general belong to the "flexible disorder" class of IDPs (52), wherein amino acid patterns that generate intrinsic disorder are conserved, but amino acid sequence per se, is not (61). Moreover, although these proteins all clearly contain regions of low-complexity sequence (11, 13, 44) their conserved features include not only their intrinsic disorder, but also their propensity for LLPS (Fig. 6A, *SI Appendix*, Fig. S14). These two properties, although related, are not directly correlated (49, 50, 54). In particular, a preponderance of aromatic and non-aromatic π-π planar contacts and charge-dense or charge-repeat regions drive LLPS (50, 54) and these features are consistently found in clock repressors, particularly FRQ. The similar amino acid compositions of these proteins may then potentially give rise to their shared function. Moreover, extensive phosphorylation may promote LLPS because it increases extended states, solvation of the peptide backbone, charge density and intermolecular hydrogen bonding capacity (49, 50, 54). For FRQ, the sequence predictions are borne out experimentally, with p-FRQ having a greater tendency to phase-separate than np-FRQ. It is remarkable that p-FRQ, despite being more soluble, dynamic and less aggregated than np-FRQ, also phase separates more readily across a broad temperature range.

Live cell imaging of fluorescently-tagged FRQ proteins provides support for FRQ phase separation in *N. crassa* nuclei. The concentrated foci observed at specific positions in the nuclei indicate condensate behavior, similar to that observed for other phase separating proteins (21, 22, 55-57). Ongoing experiments are exploring more deeply the spatiotemporal dynamics of FRQ condensates in nuclei. Of particular interest is drawing comparisons between FRQ and the Drosophila Period protein, which has been observed in similar foci that change in size and subnuclear localization throughout the circadian cycle (21).

Phosphorylation is known to modulate LLPS in other systems, but the effects are variable. For example, phosphorylation of the transcriptional silencing factor HP1α also enhances LLPS, whereas only the non-phosphorylated form of xenopus CPEB4 involved in translation of mRNA poly-A tails undergoes LLPS (27, 62). FRQ, especially p-FRQ, may achieve its inhibitory function by sequestering the FFC and WCC into membraneless organelles. The large, disordered domains and capacity for multi-valency of the WC proteins (13) may also facilitate their partitioning into such condensates. In the fly clock, PER and the WCC analog CLK, produce liquid-like foci in the nuclei that are most prevalent during the repressive phase of the circadian cycle (21). These large foci, which are few and localized to the nuclear periphery, may serve to organize clock-controlled genes during repression (21). LLPS may also influence the nuclear transport of FRQ by affecting interactions with the nuclear import machinery as has been observed with proteins such as TD43 and FUS (63, 64). LLPS reduces the ability of FRQ to act as a substrate for CK1 (Fig. 7B and C), and this reactivity correlates with reduced dynamics of FRQ in the phase-separated state (Fig. 7D). In the cell, this mechanism may modulate the timing of FRQ phosphorylation, which is closely linked to clock period (17, 44). Moreover and collectively, the data from Figures 6, 7, and *SI Appendix* Fig. S19 show that as temperature increases, LLPS increases, and as LLPS increases, the ability of CK1 to phosphorylate FRQ decreases. The rate of FRQ phosphorylation dictates period length (17). Therefore, this negative feedback of temperature on period mediated by LLPS formation could provide a mechanism for circadian temperature compensation of period length. Sequestration of CK1 (and FRH) into condensates may also render these factors unavailable to target other cellular substrates. Phosphorylation alters FRQ interactions throughout the circadian cycle, not unlike the workings of the cyanobacterial clock, which relies upon a timed phospho-code to regulate enzymatic components (12, 65). We demonstrate that FRQ likewise responds to phosphorylation with non-uniform conformational changes across its sequence and an increased propensity for LLPS. It is the latter property that appears conserved among negative-arm repressor proteins in eukaryotic clocks and may thus be a critical function of their intrinsic disorder and extensive post-translational modifications.

Author contributions: D.T., N,M., B.M.B., J.C.D., A.B. and B.R.C. designed research; D.T., N.M., B.M.B., and S.C. performed research; D.T., N,M., B.M.B., S.C., J.C.D., A.B. and B.R.C. analyzed data; D.T. and B.R.C. wrote the paper with contributions and editing from all authors.
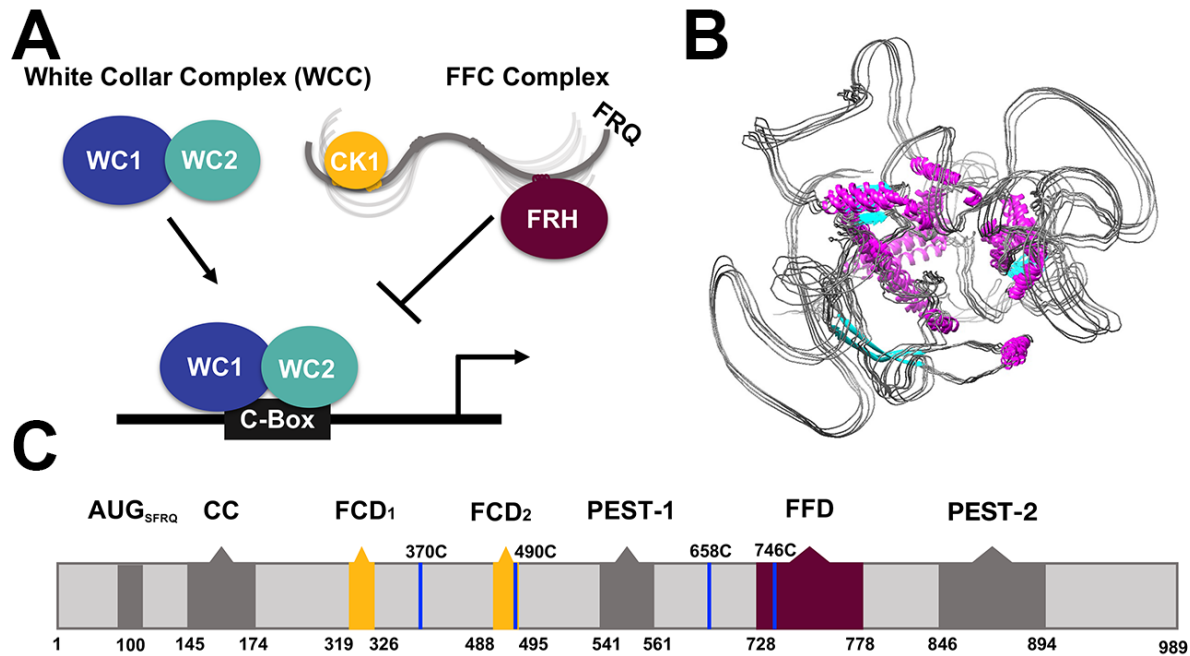
Data Availability. The mass spectrometry FRQ phosphorylation data have been deposited to the ProteomeXchange Consortium via the PRIDE partner repository with the dataset identifier PXD037938. All other data are included in the article and/or supporting Information.

15

Figure 1: FRQ is a large, dynamic component of the clock oscillator (A) The TTFL in *Neurospora crassa*. In the core circadian oscillator, **F**RQ associates with **F**RH and **C**K1 to form a repressor complex (the **FFC**) This complex inhibits the positive-acting transcription-factor known as the white-collar complex WCC, composed of WhiteCollar-1 (WC-1) and WhiteCollar-2 (WC-2). The WCC activates *frq* expression by binding to the c-box region in the *frq* promoter. Stoichiometries of the components are not represented in the schematic. (B) Several AlphaFold derived models of FRQ superimposed to highlight the conformational heterogeneity of the protein (α-helices highlighted in magenta and β-strands in cyan) (C) Functional domains of FRQ showing the start position for the S-FRQ isoform (AUG_{SFRQ}.) and the four native cysteine residues. Characterized domains include: CC - coiled coil domain, FCD - FRQ:CK1 interacting domain, PEST - proline, glutamic acid, serine, and threonine-rich domain and FFD - FRQ:FRH interacting domain.
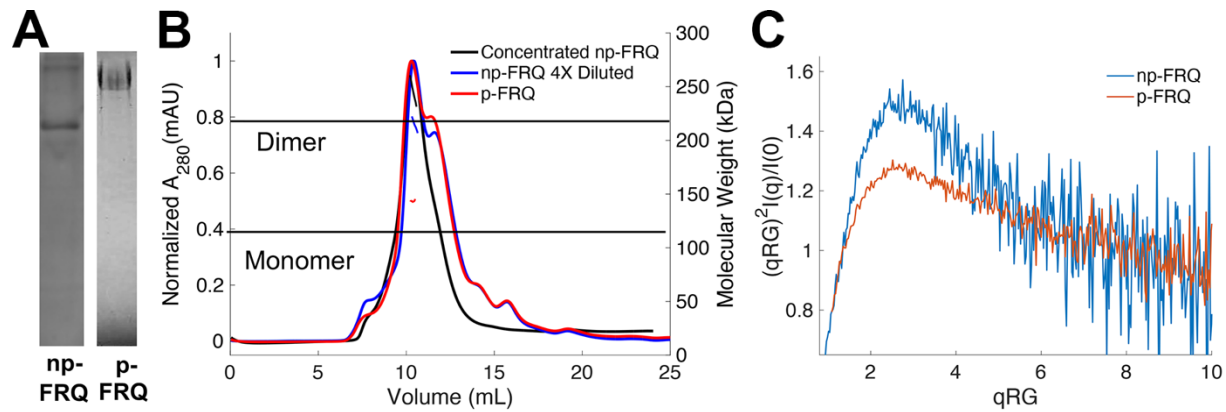
Figure 2: Purification of FRQ in non-phosphorylated and phosphorylated forms reveals IDP behavior (A) SDS-PAGE gel showing non-phosphorylated (np-FRQ) and phosphorylated FRQ (p-FRQ). Both samples represent the full-length long isoform (L-FRQ, residues 1-989). (B) Size exclusion chromatography–multiangle light scattering (SEC-MALS) of phosphorylated FRQ (p-FRQ) and non-phosphorylated (np-FRQ). The molecular weight (MW) of p-FRQ (~143 ± 1 kDa) is somewhat larger than that of a monomer (~110 kDa), but substantially smaller than that of a dimer, whereas the high concentration MW value of np-FRQ (~261 ± 1 kDa) is slightly larger than that expected for a dimer. (C) Dimensionless Kratky plot of SAXS data for p-FRQ and np-FRQ, in both cases the peak positions of the curves are shifted from that expected for a globular protein ($\sqrt{3}$,1.104), but neither plateau at 2, which would be characteristic of a flexible, denatured polypeptide (31). See Table S1 for additional SAXS parameters.

17
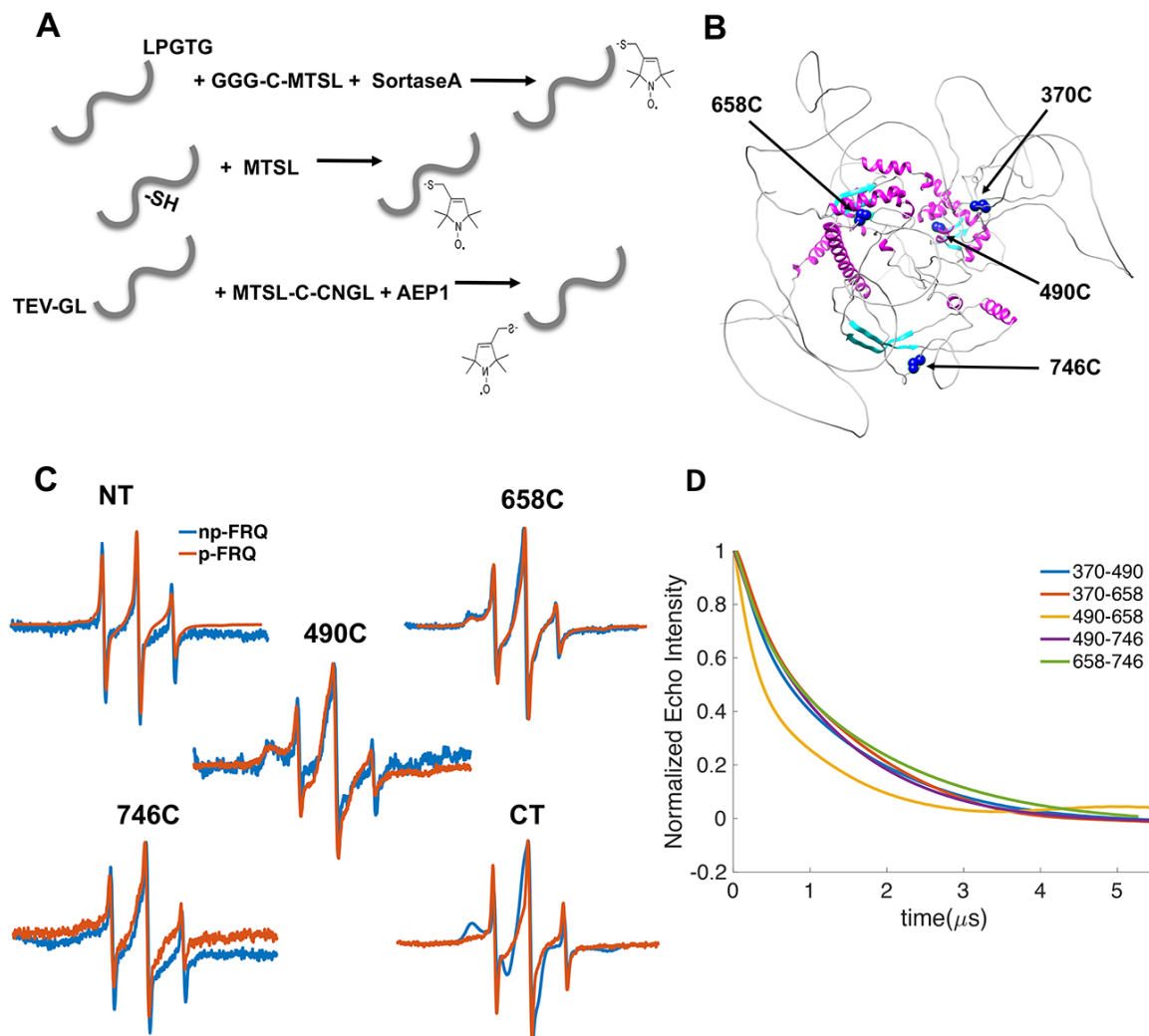
Figure 3: ESR spectroscopy studies of spin-labeled FRQ. (A) Spin-labeling strategies for FRQ. MTSL was used for internal labeling of cysteine residues and AEP1 and SortaseA were used to label the N and C terminus, respectively. (B) AlphaFold generated model of FRQ with the postions of native spin-labeled cysteine residues highlighted in dark blue. (C) X-band (9.8 GHz) room temperature cw-ESR measurements for various spin-labeled FRQ variants, each containing a single Cys labeling site, as designated. Data represented as first-derivative spectra with the horizontal axes depicting the static field strength (typically 3330 to 3400 G), and the vertical axis depicting the change in magnetic susceptibility with respect to the static field, in arbitrary units. (D) Time-domain data of DEER measurements for double-cysteine labeled FRQ variants. The baseline-corrected time domain dipolar evolution traces are shown after denoising; unprocessed traces are given in Supplemental *SI Appendix*, Fig. S5. The 490-658 separation is noticeably closer and more ordered than the others.
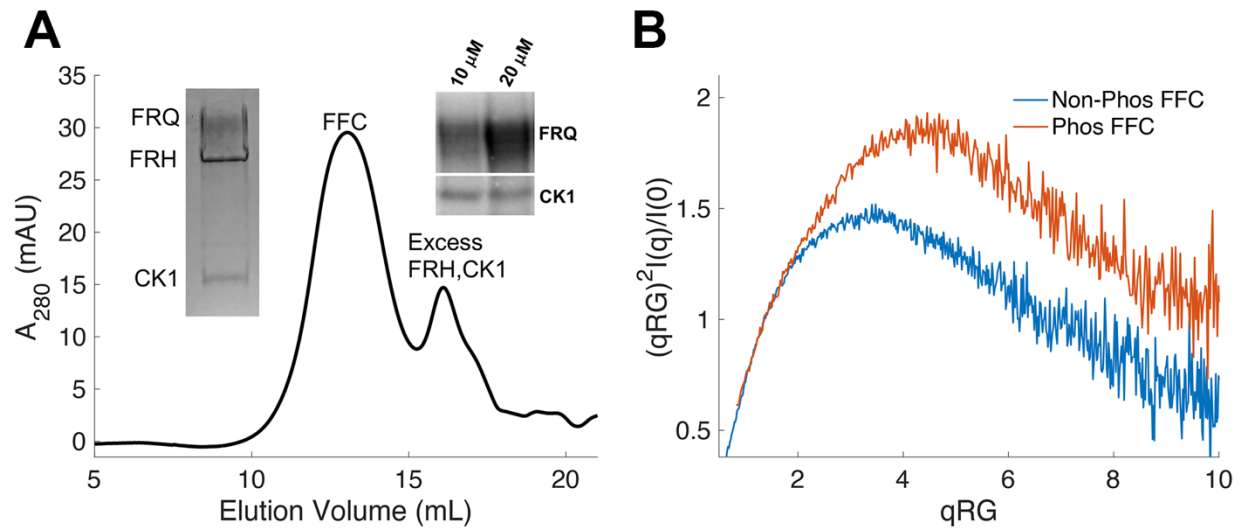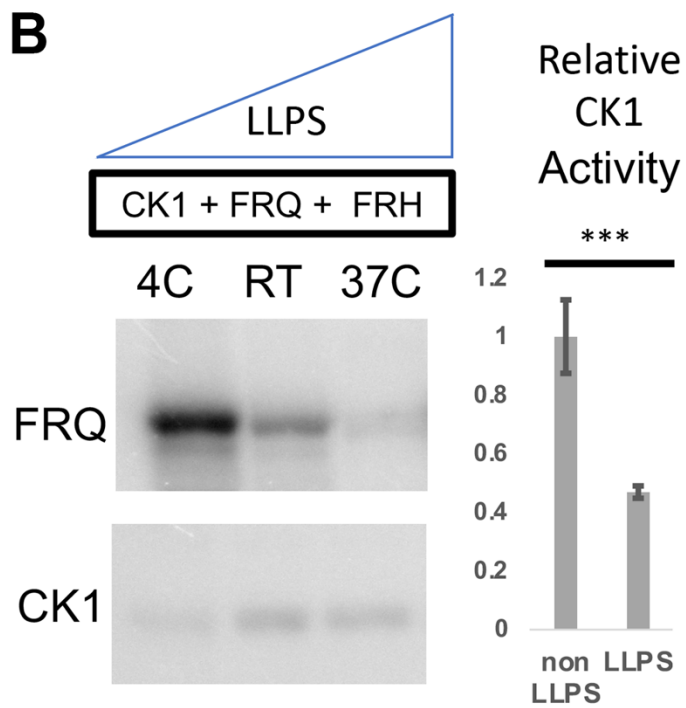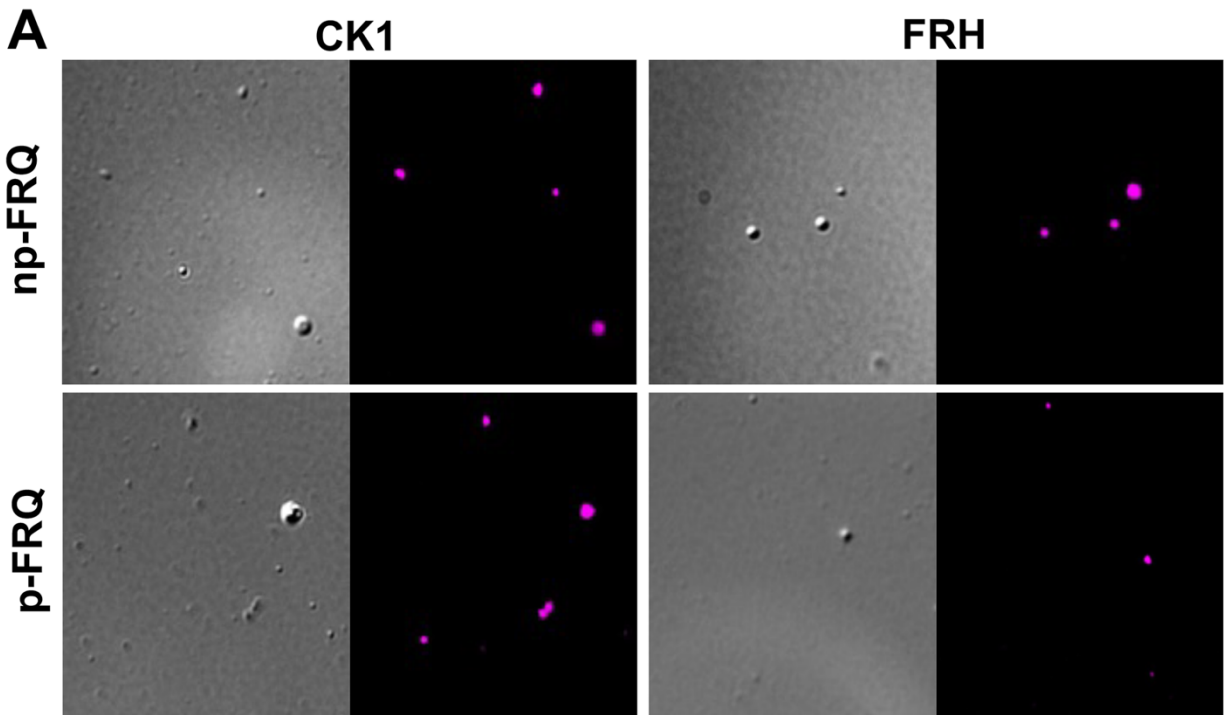
Figure 4: Properties of the FFC. (A) SEC of the FFC ; left inset: SDS-PAGE gel inset of the components; right inset: ^{32}P-autoradiogram of FRQ phosphorylation by CK1 and CK1 autophosphorylation at 10 and 20 μM FRQ all in the presence of FRH. Complete autoradiograms are shown in *SI Appendix*, Fig. S12 . (B) Overlay of dimensionless Kratky plots of SAXS data from the FFC formed with either np- or p-FRQ. The SAXS-derived MW of np-FRQ FFC = 285 kDa, which compares to a predicted value of 273 kDa; MW of p-FFC = 340 kDa; *SI Appendix* Table S1).
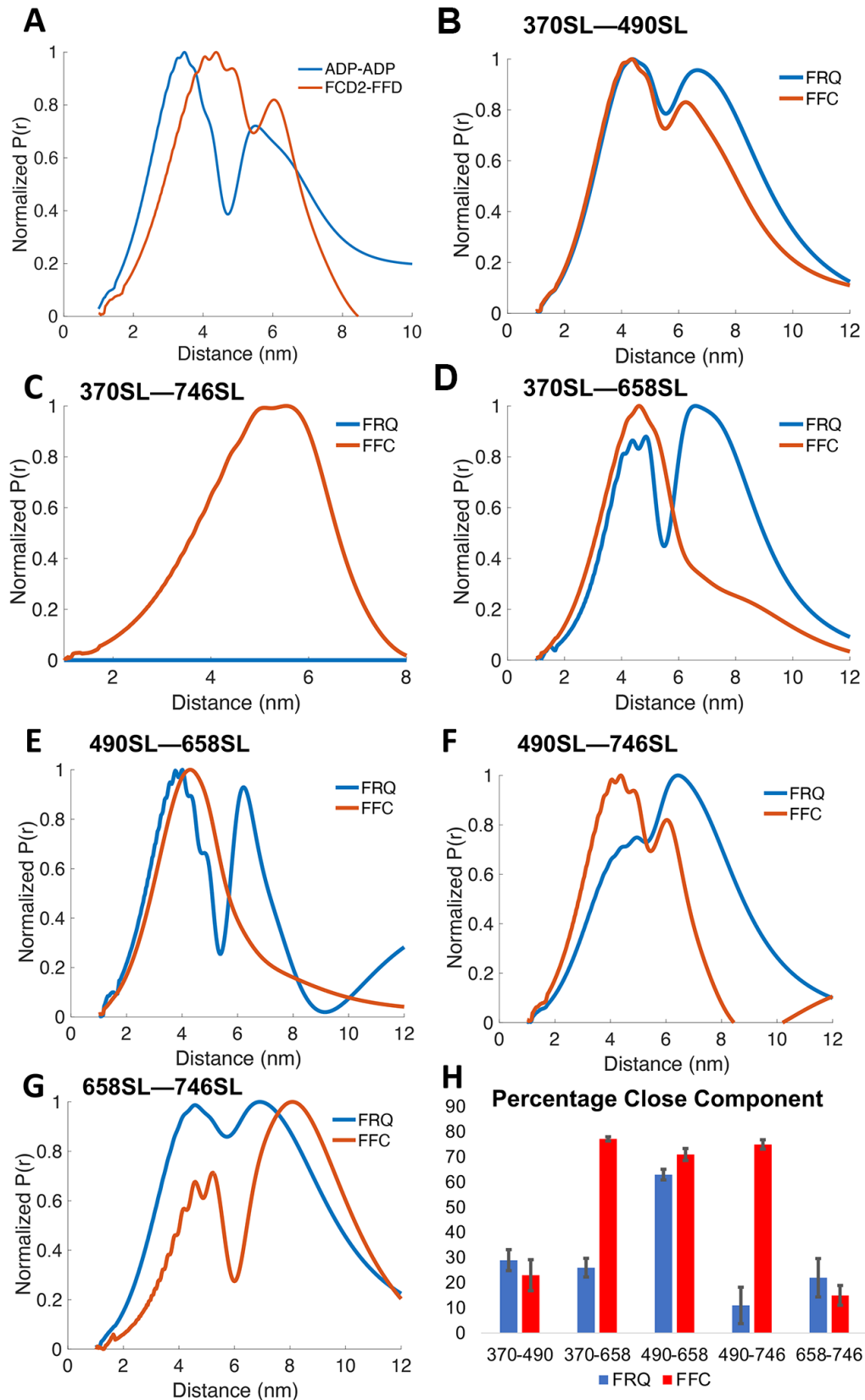
Figure 5: PDS distance distributions of spin-labeled FRQ and the FFC. (A) DEER-derived distance distributions of the FFC wherein the spins were directed by ADP linkage to target the FRH and CK1 ATP-binding sites (blue) or in the form of MTSL labeling of cysteine residues within the FCD2 and FFD domains of FRQ (red). Time-domain data and distance distributions with error estimates are shown in *SI Appendix*, Fig. S6-S10. (B-G) DEER-derived distance distributions of cysteine residue pairs labeled with MTSL within p-FRQ, either alone (blue) or within the FFC (red). (H) The proportion of the closer distance peak in the distance distributions of (A) in FRQ (blue) or FRQ+FRH+CK1(FFC) (red) samples. The error bars reflect the uncertainty in estimating the population of each peak and were derived from analyses shown in *SI Appendix*, Fig. S8 and S9. In these experiments, only FRQ was labeled with MTSL at the positions noted.
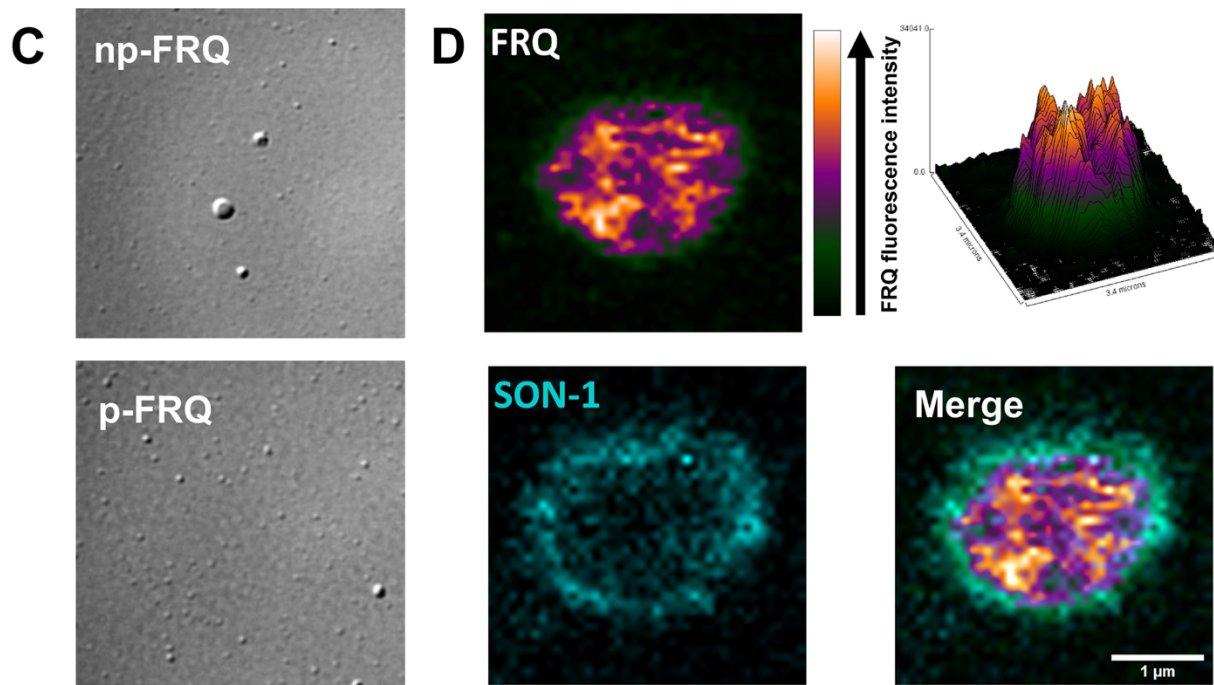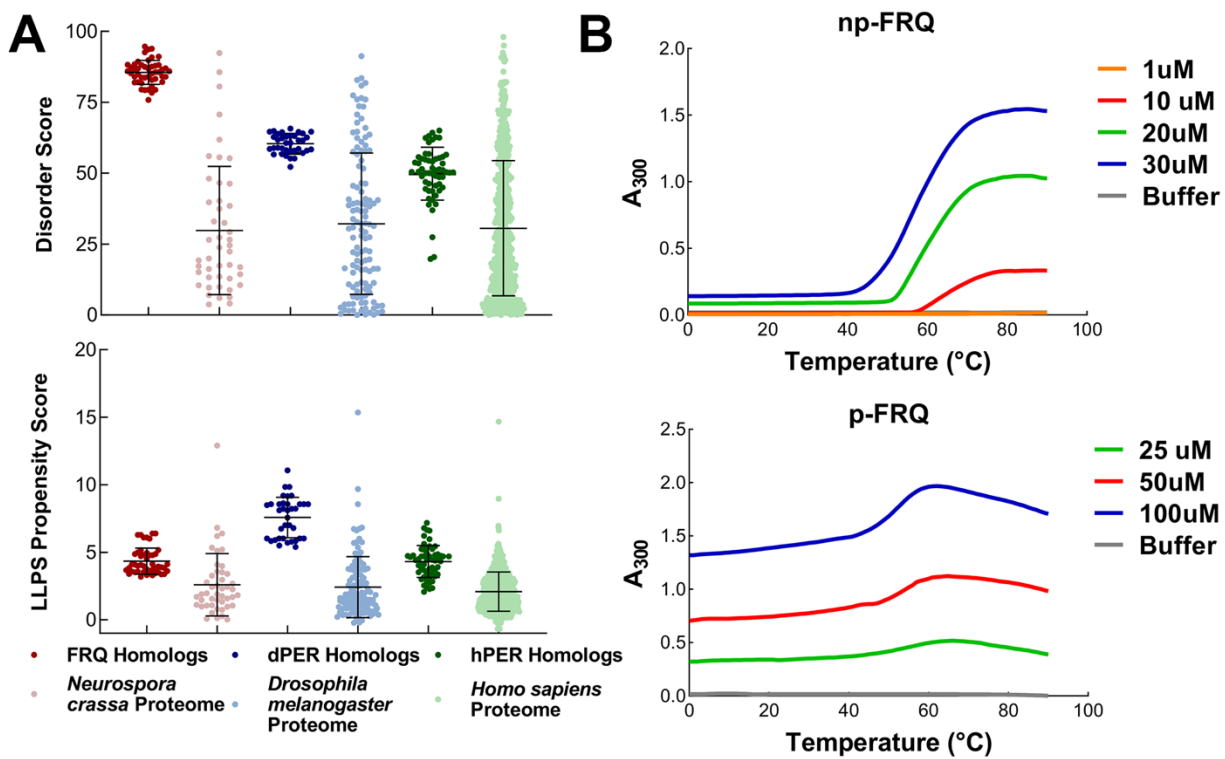
Figure 6: FRQ undergoes LLPS in agreement with predictions from its sequence properties and those of its functional analogs. (A) IUPred2A disorder predictions and LLPS propensity predictions using "Pi-Pi" are shown for FRQ (red), dPER1 (blue) and hPER1 (green) as compared to values for proteins of similar length from their respective proteomes. The mean and standard deviations are represented as horizontal and vertical black bars, respectively. (B) UV-Vis absorption spectrum of p-FRQ and np-FRQ as a function of temperature at increasing concentrations. (C) Microscopy images of 20 μM p-FRQ and np-FRQ in 500 mM KCl, 20 mM Na_2HPO_4, pH 7.4 at 25 °C; images shown at 100x magnification. (D) Live cell fluorescent imaging of FRQ[mNeonGreen] in nuclei of *Neurospora* hyphae. Upper left panel shows the FRQ channel, represented as a multicolor heat map of fluorescence intensity; Upper right panel shows a surface plot derived from the raw FRQ image to emphasize regions of concentration; lower left shows nucleoporin SON-1[mApple], which localizes to the cytoplasmic face of the nuclear envelope; bottom left shows the FRQ:SON-1 merge image. The images were acquired on a Zeiss 880 laser scanning confocal microscope and were smoothed by bicubic interpolation during 10-fold enlargement from 42 X 42 pixels to 420 X 420 pixels.
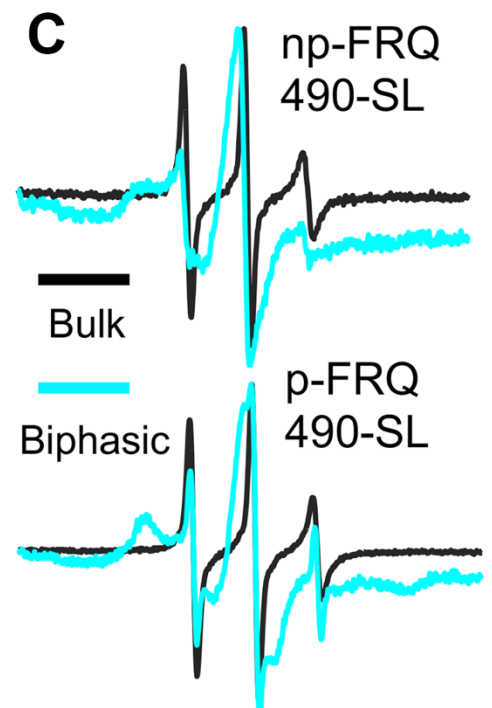
Figure 7: LLPS alters the structural and enzymatic properties of the FFC. (A) Differential Interference Contrast (DIC) microscopy images at 25 °C of phase-separated, np-FRQ droplets (20μM) in 500 mM KCl, 20mM Na_2HPO_4, pH 7.4 with either Cy5-labeled FRH or CK1 visualized using Cy-5 fluorescence (B) Autoradiography of FRQ (20 μM) (left) phosphorylated by CK1 in the presence of FRH at increasing temperatures. The complete autoradiograms are shown in *SI Appendix*, Fig. S13. Quantification of the radio-assay shown at right with phosphorylation levels under non-LLPS conditions normalized to 1. Note: *** denotes a p-value << 0.05. (C) X- band (9.8GHz) RT cw-ESR spectra of FRQ labeled with MTSL at the 490 site in solubilizing buffer (black) and under conditions that promote LLPS (cyan). Data represented as first-derivative spectra with the horizontal axes depicting the static field strength (typically 3330 to 3400 G), and the vertical axis depicting the change in magnetic susceptibility with respect to the static field, in arbitrary units.

References:

1. J. M. Hurley, J. J. Loros, J. C. Dunlap, Circadian Oscillators: Around the Transcription-Translation Feedback Loop and on to Output. *Trends in Biochemical Sciences* **41**, 834-846 (2016).

2. B. R. Crane, M. W. Young, Interactive Features of Proteins Composing Eukaryotic Circadian Clocks. *Annual Review of Biochemistry* **83**, 191-219 (2014).

3. J. Cha, M. Zhou, Y. Liu, Mechanism of the Neurospora Circadian Clock, a FREQUENCY-centric View. *Biochemistry* **54**, 150-156 (2014).

4. J. C. Dunlap, J. J. Loros, Making Time: Conservation of Biological Clocks from Fungi to Animals. *Microbiology Spectrum* **5**, 3 (2017).

5. J. M. Hurley, L. F. Larrondo, J. J. Loros, J. C. Dunlap, Conserved RNA Helicase FRH Acts Nonenzymatically to Support the Intrinsically Disordered Neurospora Clock Protein FRQ. *Molecular Cell* **52**, 832-843 (2013).

6. K. S. Conrad *et al.*, Structure of the frequency-interacting RNA helicase: a protein interaction hub for the circadian clock. *EMBO J.* **35**, 1707-1719 (2016).

7. A. C. Froehlich, Y. Liu, J. J. Loros, J. C. Dunlap, White collar-1, a circadian blue light photoreceptor, binding to the frequency promoter. *Science* **297**, 815-819 (2002).

8. M. Zhou *et al.*, Non-optimal codon usage affects expression, structure and function of clock protein FRQ. *Nature* **495**, 111-115 (2013).

9. A. Diernfellner *et al.*, Long and short isoforms of Neurospora clock protein FRQ support temperature-compensated circadian rhythms. *Febs Letters* **581**, 5759-5764 (2007).

10. Y. Liu, N. Y. Garceau, J. J. Loros, J. C. Dunlap, Thermally regulated translational control of FRQ mediates aspects of temperature responses in the Neurospora circadian clock. *Cell* **89**, 477-486 (1997).

11. J. M. Hurley, L. F. Larrondo, J. J. Loros, J. C. Dunlap, Conserved RNA helicase FRH acts nonenzymatically to support the intrinsically disordered neurospora clock protein FRQ. *Molecular Cell* **52**, 832-843 (2013).

12. B. Wang, A. N. Kettenbach, X. Zhou, J. J. Loros, J. C. Dunlap, The Phospho-Code Determining Circadian Feedback Loop Closure and Output in Neurospora. *Molecular Cell* **74**, 771-784.e773 (2019).

13. J. F. Pelham, J. C. Dunlap, J. M. Hurley, Intrinsic disorder is an essential characteristic of components in the conserved circadian circuit. *Cell Communication and Signaling* **18** (2020).

14. J. C. Dunlap, J. J. Loros, Just-So Stories and Origin Myths: Phosphorylation and Structural Disorder in Circadian Clock Proteins. *Molecular Cell* **69**, 165-168 (2018).

15. C. L. Baker, A. N. Kettenbach, J. J. Loros, S. A. Gerber, J. C. Dunlap, Quantitative Proteomics Reveals a Dynamic Interactome and Phase-Specific Phosphorylation in the Neurospora Circadian Clock. *Molecular Cell* **34**, 354-363 (2009).

16. X. Liu *et al.*, FRQ-CK1 interaction determines the period of circadian rhythms in Neurospora. *Nature Communications* **10**, 4352 (2019).

17. L. F. Larrondo, C. Olivares-Yañez, C. L. Baker, J. J. Loros, J. C. Dunlap, Decoupling circadian clock protein turnover from circadian period determination. *Science* **347**, 1257277 (2015).

18. G. L. Dignon, R. B. Best, J. Mittal, Biomolecular Phase Separation: From Molecular Driving Forces to Macroscopic Properties. *Annual Review of Physical Chemistry* **71**, 53-75 (2020).

19. P. E. Wright, H. J. Dyson, Intrinsically disordered proteins in cellular signalling and regulation. *Nature Reviews Molecular Cell Biology* **16**, 18-29 (2014).

20. J. H. Jung *et al.*, A prion-like domain in ELF3 functions as a thermosensor in Arabidopsis. *Nature* **585**, 256-260 (2020).

21. Y. B. Xiao, Y. Yuan, M. Jimenez, N. Soni, S. Yadlapalli, Clock proteins regulate spatiotemporal organization of clock genes to control circadian rhythms. *Proc. Natl. Acad. Sci. USA* **118**, e2019756118 (2021).

22. B. M. Bartholomai, A. S. Gladfelter, Loros, J. J., J. C. Dunlap, PRD-2 mediates clock-regulated perinuclear localization of clock gene RNAs within the circadian cycle of Neurospora. *Proc. Natl. Acad. Sci. USA* **119**, e2203078119 (2022).

23.   J. Jumper *et al.*, Highly accurate protein structure prediction with AlphaFold. *Nature 2021 596:7873* **596**, 583-589 (2021).

24.   V. Muñoz, L. Serrano, Elucidating the folding problem of helical peptides using empirical parameters. *Nature Structural Biology* **1**, 399-409 (1994).

25.   L. Lauinger, A. Diernfellner, S. Falk, M. Brunner (2014) The RNA helicase FRH is an ATP-dependent regulator of CK1a in the circadian clock of Neurospora crassa. in *Nature communications*.

26.   C. P. Pedersen, P. Seiffert, I. Brakti, K. Bugge, Production of intrinsically disordered proteins for biophysical studies: Tips and tricks. *Methods in Molecular Biology* **2141**, 195-209 (2020).

27.   M. Seal *et al.*, Evolution of CPEB4 Dynamics Across its Liquid–Liquid Phase Separation Transition. *The Journal of Physical Chemistry B* **125**, 12947-12957 (2021).

28.   C. Querfurth *et al.*, Circadian Conformational Change of the Neurospora Clock Protein FREQUENCY Triggered by Clustered Hyperphosphorylation of a Basic Domain. *Molecular Cell* **43**, 713-722 (2011).

29.   C. T. Tang *et al.*, Setting the pace of the Neurospora circadian clock by multiple independent FRQ phosphorylation events. *Proc. Natl. Acad. Sci. USA* **106**, 10722-10727 (2009).

30.   J. Trewhella *et al.*, 2017 publication guidelines for structural modelling of small-angle scattering data from biomolecules in solution: An update. *Acta Crystallographica Section D: Structural Biology* **73**, 710-728 (2017).

31.   D. Durand *et al.*, NADPH oxidase activator p67phox behaves in solution as a multidomain protein with semi-flexible linkers. *Journal of Structural Biology* **169**, 45-53 (2010).

32.   A. Sagar, D. Svergun, P. Bernado, "Structural Analyses of Intrinsically Disordered Proteins by Small-Angle X-Ray Scattering" in INTRINSICALLY DISORDERED PROTEINS: Methods and Protocols*, B. B. Kragelund, K. Skriver, Eds. (2020), vol. 2141, pp. 249-269.

33.   E. W. Martin, J. B. Hopkins, T. Mittag, Small-angle X-ray scattering experiments of monodisperse intrinsically disordered protein samples close to the solubility limit. *Methods in Enzymology* **646**, 185-222 (2021).

34.   D. Durand *et al.*, NADPH oxidase activator P67(phox) behaves in solution as a multidomain protein with semi-flexible linkers. *Journal of Structural Biology* **169**, 45-53 (2010).

35.   R. P. Rambo, J. A. Tainer, Characterizing Flexible and Intrinsically Unstructured Biological Macromolecules by SAS Using the Porod-Debye Law. *Biopolymers* **95**, 559-571 (2011).

36.   L. J. Berliner, J. Grunwald, H. O. Hankovszky, K. Hideg, A novel reversible thiol-specific spin label - papain active-site labeling and inhibition. *Analytical Biochemistry* **119**, 450-455 (1982).

37.   S. Chandrasekaran *et al.*, Tuning flavin environment to detect and control light-induced conformational switching in Drosophila cryptochrome. *Communications Biology 2021 4:1* **4**, 1-12 (2021).

38.   G. K. T. Nguyen, Y. Cao, W. Wang, C. F. Liu, J. P. Tam, Site-Specific N-Terminal Labeling of Peptides and Proteins using Butelase 1 and Thiodepsipeptide. *Angewandte Chemie-International Edition* **54**, 15694-15698 (2015).

39.   J. H. Freed (2005) ESR and Molecular Dynamics. in *Biomedical EPR, Part B: Methodology, Instrumentation, and Dynamics* (Springer, Boston, MA), pp 239-268.

40.   J. M. Franck, S. Chandrasekaran, B. Dzikovski, C. R. Dunnam, J. H. Freed, Focus: Two-dimensional electron-electron double resonance and molecular motions: The challenge of higher frequencies. *Journal of Chemical Physics* **142**, 212302 (2015).

41.   L. Emmanouilidis *et al.*, NMR and EPR reveal a compaction of the RNA-binding protein FUS upon droplet formation. *Nature Chemical Biology 2021 17:5* **17**, 608-614 (2021).

42.   A. Bonucci, M. G. Murrali, L. Banci, R. Pierattelli, A combined NMR and EPR investigation on the effect of the disordered RGG regions in the structure and the activity of the RRM domain of FUS. *Scientific Reports* **10**, 1-13 (2020).

43.   W. L. Hubbell, D. S. Cafiso, C. Altenbach, Identifying conformational changes with site-directed spin labeling. *Nature Structural Biology* **7**, 735-739 (2000).

44.   D. Marzoll, F. E. Serrano, A. Shostak, C. Schunke, A. C. R. Diernfellner, Casein kinase 1 and disordered clock proteins form functionally equivalent , phospho-based circadian modules in fungi and mammals. *Proc. Natl. Acad. Sci. USA* **119**, e2118286119 (2022).

45.   A. R. Muok, T. K. Chua, H. Le, B. R. Crane, Nucleotide Spin Labeling for ESR Spectroscopy of ATP-Binding Proteins. *Applied Magnetic Resonance* **49**, 1385-1395 (2018).

46.   P. Cheng, Q. He, Q. He, L. Wang, Y. Liu, Regulation of the Neurospora circadian clock by an RNA helicase. *Genes and Development* **19**, 234-241 (2005).

47.   J. Guo, P. Cheng, Y. Liu, Functional significance of FRH in regulating the phosphorylation and stability of Neurospora circadian clock protein FRQ. *J. Biol. Chem.* **285**, 11508-11515 (2010).

48.   A. E. Posey, A. S. Holehouse, R. V. Pappu, Phase Separation of Intrinsically Disordered Proteins. *Methods in enzymology* **611**, 1-30 (2018).

49.   B. Bolognesi *et al.*, A Concentration-Dependent Liquid Phase Separation Can Cause Toxicity upon Increased Protein Expression. *CellReports* **16**, 1-10 (2016).

50. R. M. Vernon *et al.*, Pi-Pi contacts are an overlooked protein feature relevant to phase separation. *Elife* **7**, e31486 (2018).

51. R. Somjee, D. M. Mitrea, R. W. Kriwacki (2020) Exploring Relationships between the Density of Charged Tracts within Disordered Regions and Phase Separation. in *Pacific Symposium on Biocomputing* (Hi), pp 207-218.

52. D. M. Shapiro, M. Ney, S. A. Eghtesadi, A. Chilkoti, Protein Phase Separation Arising from Intrinsic Disorder: First-Principles to Bespoke Applications. *Journal of Physical Chemistry B* **125**, 6740-6759 (2021).

53. B. Q. Liu, B. Poolman, A. J. Boersma, Ionic Strength Sensing in Living Cells. *Acs Chemical Biology* **12**, 2510-2514 (2017).

54. A. L. Szabó, A. Sánta, R. Pancsa, Z. Gáspári, Charged sequence motifs increase the propensity towards liquid–liquid phase separation. *FEBS Letters* **596**, 1013-1028 (2022).

55. E. Caragliano *et al.*, Human cytomegalovirus forms phase-separated compartments at viral genomes to facilitate viral replication. *Cell Reports* **38** (2022).

56. A. Gonzalez *et al.*, Mechanism of karyopherin-beta 2 binding and nuclear import of ALS variants FUS(P525L) and FUS(R495X). *Scientific Reports* **11** (2021).

57. R. Tatavosian *et al.*, Nuclear condensates of the Polycomb protein chromobox 2 (CBX2) assemble through phase separation. *Journal of Biological Chemistry* **294**, 1451-1463 (2019).

58. M. Kataoka, K. Kuwajima, F. Tokunaga, Y. Goto, Structural characterization of the molten globule of alpha-lactalbumin by solution X-ray scattering. *Protein Science* **6**, 422-430 (1997).

59. A. G. Kikhney, D. I. Svergun, A practical guide to small angle X-ray scattering (SAXS) of flexible and intrinsically disordered proteins. *Febs Letters* **589**, 2570-2577 (2015).

60. P. Cheng, Y. Yang, C. Heintzen, Y. Liu, Coiled-coil domain-mediated FRQ–FRQ interaction is essential for its circadian clock function in Neurospora. *EMBO J.* **20**, 101-108 (2001).

61. J. Bellay *et al.*, Bringing order to protein disorder through comparative genomics and genetic interactions. *Genome Biology* **12**, R14 (2011).

62. A. G. Larson *et al.*, Liquid droplet formation by HP1 alpha suggests a role for phase separation in heterochromatin. *Nature* **547**, 236-241 (2017).

63. F. Gasset-Rosa *et al.*, Cytoplasmic TDP-43 De-mixing Independent of Stress Granules Drives Inhibition of Nuclear Import, Loss of Nuclear TDP-43, and Cell Death. *Neuron* **102**, 339-357 (2019).

64. A. Gonzalez *et al.*, Mechanism of karyopherin-β2 binding and nuclear import of ALS variants FUS(P525L) and FUS(R495X). *Scientific Reports 2021 11:1* **11**, 1-15 (2021).

65. M. J. Rust, J. S. Markson, W. S. Lane, D. S. Fisher, E. K. O'Shea, Ordered phosphorylation governs oscillation of a three-protein circadian clock. *Science* **318**, 809-812 (2007).

Supplementary Information

Phosphorylation, disorder, and phase separation govern the behavior of FRQ in the fungal circadian clock

Daniyal Tariq[a,*], Nicole Maurici[b,*], Bradley M. Bartholomai[c], Siddarth Chandrasekaran[a], Jay C. Dunlap[c], Alaji Bah[b] and Brian R. Crane[a].

[a]Department of Chemistry & Chemical Biology, Cornell University, Ithaca, NY,14853;
[b]Department of Biochemistry and Molecular Biology, SUNY Upstate Medical University, Syracuse, NY, 13210;
[c]Department of Molecular and Systems Biology, Geisel School of Medicine at Dartmouth, Hanover, NH 03755.
*Denotes equal contribution

Contents

Materials and Methods:

Protein Expression and Purification

Full length L-FRQ (Uniprot ID:P19970), CK1 (CK1a; Uniprot ID:V5IR38) and FRHΔN (residues 100-1106) (Uniprot ID:Q1K502) were sub-cloned into a pET28a vector (Novagen) bearing an N-terminal His$_6$-tag and kanamycin resistance. Note: L-FRQ contained the S513A substitution to improve protein stability as noted in (1). The plasmids encoding the proteins were transformed into BL21 (DE3) *E. coli* cells, grown in LB media containing 50 µg ml^{-1} kanamycin to an optical density (OD$_{600}$) of ~0.6–0.8 at 37 °C and induced with 1 mM IPTG at 17 °C or room temperature. Cells were harvested after 12–18 h by centrifugation at 5,000 rpm. and 4 °C. FRH and CK1 were purified by standard Ni-NTA chromatography followed by ion-exchange and size-exclusion chromatography. Briefly, cells were resuspended in lysis buffer (50 mM Tris pH 8.0, 500 mM NaCl, 10% glycerol, 1 mM MgCl$_2$, 5 mM imidazole) and sonicated on ice. The lysate was clarified by centrifugation at 20,000 rpm for 1 hr. The clarified lysate was applied to a gravity Ni-NTA column and washed with 5 column volumes (CVs) of wash buffer (50 mM Tris pH 8.0, 500 mM NaCl, 10% glycerol, 1 mM MgCl$_2$, 20 mM imidazole.) The protein was eluted using the elution buffer (50 mM Tris pH 8.0, 500 mM NaCl, 10% glycerol, 1 mM MgCl$_2$, 500 mM imidazole). The protein was then diluted into IEX (ion-exchange) bufferA (50 mM HEPES pH 7.5, 10% glycerol), applied to an S cation exchange column (GE Healthcare) and eluted over a 20 CV gradient against IEX bufferB (50 mM HEPES pH 7.5, 1 M NaCl, 10% glycerol). Fractions containing the protein were pooled, concentrated, and run over an S200 26/60 gel-filtration column pre-equilibrated in gel-filtration buffer (GFB; 50 mM HEPES, 200 mM NaCl, 10% glycerol.) L-FRQ was purified under denaturing conditions. Cells were resuspended in lysis buffer (50 mM Na$_2$PO$_4$ pH 7.42, 300 mM NaCl, 5 mM imidazole, 4 M guanidinium hydrochloride (GuHCl)) and sonicated on ice. The lysate was clarified by centrifugation at 20,000 rpm for 1 hr. The clarified lysate was applied to a gravity Ni-NTA column and washed with 3 CV of lysis buffer. The protein was eluted using the elution buffer (50 mM Na$_2$PO$_4$ pH 7.42, 300 mM NaCl, 500 mM imidazole, 4 M GuHCl). The protein was concentrated and applied to a S200 26/60 gel-filtration column pre-equilibrated in 50 mM Na$_2$PO$_4$ pH 7.42, 300 mM NaCl, 5mM Imidazole, 4 M GuHCl. Fractions containing the protein were pooled and concentrated. The concentrated protein was flash-frozen and stored at -80 °C. Prior to experiments, the purified L-FRQ was exchanged into a non-denaturing buffer (50

mM Na_2PO_4 pH 7.42, 300 mM NaCl, 200 mM arginine, 10% glycerol). For FFC preparations, GFB (50 mM HEPES pH 7.42, 200 mM NaCl, 10% glycerol) was used.

SEC-MALS

Protein samples at 100 uM were injected onto a Superose-6 (GE Lifesciences), equilibrated with 50 mM HEPES pH 7.5, 200 mM NaCl. The gel filtration column was coupled to a static 18-angle light scattering detector (DAWN HELEOS-II) and a refractive index detector (Optilab T-rEX) (Wyatt Technology, Goleta, CA). Data were collected every second at a flow rate of 0.5 ml/min and analysis was carried out using ASTRA VI, yielding the molar mass and mass distribution (polydispersity) of the sample. The monomeric fraction of BSA (Sigma, St. Louis, MO) was used to standardize the light scattering detectors and optimize data quality control.

SEC-SAXS

X-ray scattering experiments were performed at the Cornell High Energy Synchrotron Source (CHESS) G1 station. Size-exclusion chromatography-coupled SAXS (SEC–SAXS) experiments were performed using a Superdex 200 5/150 GL or Superose-6 5/150 GL (3 mL) column operated by a GE AKTA Purifier at 4 °C with the elution flowing directly into an in-vacuum X-ray sample cell. Samples were centrifuged at 14,000×g for 10 min at 4 °C before loading onto a column pre-equilibrated in a matched buffer. Samples were eluted at flow rates of 0.05–0.1 mL min^{-1}. For each sample, 2-s exposures were collected throughout elution until the elution profile had returned to buffer baseline, and scattering profiles of the elution buffer were averaged to produce a background-subtracted SEC–SAXS dataset. The scattering data was processed in RAW (2) and regions with homogenous R_G values were chosen for the Guinier and Kratky analyses.

Protein Labeling for ESR spectroscopy and microscopy experiments

Sort/AEP1-tagged FRQ was cloned into a pET28a (Novagen) vector as described in (3). The production of the sortaseA and AEP1 enzymes and their associated peptides (GGGGC for Sortase A and CNGL for AEP1) is also described in (3) and (4), respectively. To enzymatically label FRQ with either SortaseA or AEP1, 1:1 protein and SortaseA/AEP1 as well as 2x excess peptide were incubated overnight to allow the reaction to reach completion. The following day, the reaction was run on a Superpose 6 10/300 analytical SEC column to remove unreacted peptide and enzyme, and the protein containing fractions were pooled and concentrated. To prepare the ADP-β-S-SL samples, ADP-β-S-SL was synthesized as previously reported in (5). 100 μL of buffer containing 100 μM of ADP-β-S-SL and 100 μM FRH or CK1 were incubated overnight and then washed with GFB (50 mM HEPES pH 7.42, 200 mM NaCl, 10% glycerol) through 5x dilution followed by re-concentration to remove any unbound ADP-β-S-SL. 30 μL of each sample were used for data collection. For MTSL labeling, the protein was incubated with 5x molar excess of MTSL overnight to allow the reaction to reach completion. The following day, the reaction was run on HiTrap Desalting column (GE Life Sciences) to remove any excess spin-label.

To prepare fluorophore labeled FRH and CK1, the purified proteins were incubated with 2x molar excess cy5-maleimide dye (GE Life Sciences) overnight to label any accessible cysteines on the target proteins. The excess dye was removed by running the reaction over a HiTrap desalting column.

ESR Spectroscopy

The cw-ESR spectra were obtained on a Bruker E500 ESR spectrometer operating at X-band (~9.4 GHz). The ESR measurements were carried out at room temperature with a modulation amplitude of 0.5-2 G and modulation frequency of 100 kHz. All spectra were digitized to 1024 points with a sweep width of ~100 G and an average of 4–16 scans. The δ values were calculated using the display distance function on the Bruker Xepr 2.6b software.

For 4-pulse-DEER, the samples were exchanged into deuterated buffer containing 30% d8-glycerol, checked by cwESR and plunge frozen into liq. N$_2$. The pulse ESR measurements were carried out at Q-band (~34 GHz) on a Bruker E580 spectrometer equipped with a 10 W solid state amplifier (150W equivalent TWTA) and an arbitrary waveform generator (AWG). DEER was carried out using four pulses (π/2-τ1-π-τ1-πpump-τ2-π-τ2-echo) with 16-step phase cycling at 60

34

K. The pump and probe pulses were separated by 56 MHz (~20 G). The DEER data was background subtracted with an exponential background and the distance reconstruction was carried out using denoising and the SVD method (6, 7).

DIC and Fluorescence Microscopy

Cysteine-less (Cys-less) FRQ was created in order to minimize disulfide cross-linking at the high protein concentrations needed for *in vitro* phase separation experiments. For this, all four of the native cysteine residues were substituted to serine using standard molecular biology techniques. For the phase separation experiments, this cys-less FRQ variant was purified and concentrated to ~20-30 μM. Phase separation was induced via overnight dialysis into 20 mM Na_2HPO_4 (pH 7.42), 500 mM KCl. Images were taken on the Zeiss Axio Imager Z1 Upright Trinocular Fluorescence Microscope at 100x magnification. To test the interaction of FRQ with FRH and CK1, the phase separated FRQ was spiked with cy5-labeled FRH/CK1.

Turbidity assays

Cys-less FRQ (~20-30 μM) was dialyzed overnight into 20 mM Na_2HPO_4 (pH 7.42), 500 mM KCl at 4°C to induce phase separation. Absorbance at 300 nm as a function of temperature was recorded by an Agilent Cary 3500 UV-Vis Multicell Peltier using a temperature ramp rate of 5 °C/min increasing from 0°C to 100°C.

In vitro phosphorylation assay

22 μL samples containing 10-20 μM L-FRQ were incubated in the presence or absence of 2 μM CK1 and 2 μM FRH in 50 mM Na_2HPO_4 (pH 7.5), 300 mM NaCl, 200 mM arginine, 10 mM $MgCl_2$. 2 μL of 2.5 mM cold ATP and 0.1 μM of [γ-32P] ATP (3000 Ci/mmol, PerkinElmer) was added to produce a total volume of ~25 μL. After ~1h of incubation, the reaction was quenched with 25 μL of 4x SDS with 10 mM EDTA (pH 8.0) and then subjected to gel electrophoresis on a 4–20% gradient Tris-glycine gel. The gel was dried with a GelAir dryer (Bio-Rad) and placed in an imaging cassette for at least 16 h and then imaged with a phosphorimager (GE, Typhoon FLA 7000). Band intensities we quantified using the Fiji software.

Mass Spectrometry and phospho-peptide analysis

Phosphorylated FRQ was run on a 4-20% tris-glycine SDS-PAGE gel and the corresponding band was excised and trypsin digested. The digests were reconstituted in 0.5% formic acid (FA) for nanoLC-ESI-MS/MS analysis. The analysis was carried out using an Orbitrap Fusion^{TM} Tribrid^{TM} (Thermo-Fisher Scientific, San Jose, CA) mass spectrometer equipped with a nanospray Flex Ion Source, and coupled with a Dionex UltiMate 3000 RSLCnano system (Thermo, Sunnyvale, CA). The peptide samples (5 µL) were injected onto a PepMap C-18 RP nano trapping column (5 µm, 100 µm i.d x 20 mm) and then separated on a PepMap C-18 RP nano column (2 µm, 75 µm x 25 cm) at 35 °C. The Orbitrap Fusion was operated in positive ion mode with spray voltage set at 1.5 kV and source temperature at 275°C. External calibration for FT, IT and quadrupole mass analyzers was performed. In data-dependent acquisition (DDA) analysis, the instrument was operated using FT mass analyzer in MS scan to select precursor ions followed by 3 second "Top Speed" data-dependent CID ion trap MS/MS scans at 1.6 m/z quadrupole isolation for precursor peptides with multiple charged ions above a threshold ion count of 10,000 and normalized collision energy of 30%. MS survey scans at a resolving power of 120,000 (fwhm at m/z 200), for the mass range of m/z 375-1600. Dynamic exclusion parameters were set at 35 s of exclusion duration with ±10 ppm exclusion mass width. All data were acquired under Xcalibur 4.4 operation software (Thermo-Fisher Scientific). The DDA raw files with MS and MS/MS were subjected to database searches using Proteome Discoverer (PD) 2.4 software (Thermo Fisher Scientific, Bremen, Germany) with the Sequest HT algorithm. The database search was conducted against a *Neurospora Crassa* database and *E. coli* database with adding LFRQ sequence into the database. The peptide precursor tolerance was set to 10 ppm and fragment ion tolerance was set to 0.6 Da with 2 miss-cleavage allowed for either trypsin or chymotrypsin. Variable modification of methionine oxidation, deamidation of asparagines/glutamine, phosphorylation of serine/threonine/tyrosine, acetylation, M-loss and M-loss+acetylation on protein N-terminus and fixed modification of cysteine carbamidomethylation, were set for the database search. Only high confidence peptides defined by Sequest HT with a 1% FDR by Percolator were considered for confident peptide identification. All the mass spectra of phosphorylated peptides were double checked by manually inspection.

Integrated Bioinformatic Analyses and Computational Biology

All canonical protein and UniRef50 sequences for FRQ, FRH and CK1, and SWISS-Prot obtained protein sequences of *Neurospora crassa*, *Drosophila melanogaster* and *Homo sapiens*

36

were downloaded from the UniProt database (8) A combination of **(a)** in-house written Python scripts to allow us to analyze large datasets, **(b)** localCIDER (9), **(c)** IUPred2A (10), **(d)** Agadir (11), **(e)** AlphaFold 2.0 (12), **(f)** PScore (13) and (g) catGRANULE (14) were used to perform integrated bioinformatics analyses and computational biological studies of our proteins of interest. Unless mentioned, all programs were used by applying the default parameters.

Neurospora crass strain generation

Construction of the *frq[mNeonGreen]*, *son-1[mApple]* strain used for imaging was previously described (15). Briefly, a plasmid was constructed to target the endogenous *frq* locus with DNA encoding *N. crassa* codon-optimized mNeonGreen appended to the C-terminus of the *frq* ORF with a flexible linker. A gene encoding hygromycin B phosphotransferase (HPH) was introduced downstream from the 3' UTR of *frq* for selection. A plasmid was constructed containing the *N. crassa son-1* ORF with mApple appended to the C-terminus with a flexible linker for insertion at the *csr-1* locus. Transformation cassettes were amplified by PCR using NEB Q5® High-Fidelity 2X Master Mix (New England Bio Labs Cat. # M0492) and integrated into the genome by homologous recombination after electroporation of conidiophores. A homokaryotic strain containing the fluorescent fusion proteins was used for imaging.

Neurospora crassa growth

N. crassa homokaryons containing *frq[mNeonGreen]* and *csr-1::son-1[mApple]*, were grown overnight on 2% agar gel pads made with Vogel's minimal medium (16) in constant light at 25 °C. Before imaging, a section near the edge of the growing mycelium was removed and inverted on a chambered cover glass (Thermo Scientific, Cat. # 155360).

Live cell image acquisition and processing

Images were acquired using a Zeiss AxioObserver laser scanning confocal microscope with a 100X/1.46 NA Oil immersion Plan-Apochromat objective. 561 nm and 488 nm lasers were used at 2% power with 2X averaging and a gain of 800 for detection of fluorescent signals by GaAsp PMTs. Images were processed for display using FIJI (17). The cropped images displaying a single nucleus were enlarged 10X using bicubic interpolation and contrasted to the minimum and maximum gray level values. A multi-color lookup table was applied to the FRQ[mNeonGreen] channel to better observe heterogeneity of the signal and the SON-1[mApple] channel was pseudo-colored cyan to better contrast with the lookup table applied to

the FRQ[mNeonGreen] channel. The surface plot of FRQ[mNeonGreen] was generated from the raw image.

Results:

Table S1: SAXS parameters for p-FRQ, np-FRQ and their reconstitution into the FFC

	R_g [Guinier] (Å)	R_g [P(r)] (Å)	Dmax (Å)	MW [V_C] (kDa)
p-FRQ	123 ± 7	142 ± 5	530 ± 60	816
np-FRQ	100 ± 2	116 ± 4	446 ± 40	680
p-FFC	101 ± 2	136 ± 5	510 ± 20	314
np-FFC	80 ± 2	109 ± 7	480 ± 10	286

MW calculations for p-FRQ and np-FRQ are inaccurate because V_C (Volume of Correlation) plots (Integrated area of I(q)q vs q; q = 2π/d) did not converge for these species. Expected MW for LFRQ is 110 kDa. Expected FFC MW for the 1:1:1 stoichiometry of FRQ:FRH:CK1 Is 273 kDa. Errors in Dmax were estimated from the range for which P(r) tailed to zero in the high distance range without constraint.

Table S2: FRQ Cysteine residue locations and context

Site	Domain	Binding Partner at this region	Reference
370C	N/A		
490C	FCD2	CK1	(18)
658C	N/A		
746C	FFD	FRH	(19)

Table S3: FRQ regions that bind clock proteins

Binding Partner	Region	Cysteine residue(s) present in this region	Reference
FRH	695-778	746C	(19)
CK1	319-326; 488-495	490C	(18)
WC2		490C,658C,746C	(20)

Table S4: δ values from the cw-ESR central peak for FRQ variants of Fig. 3C
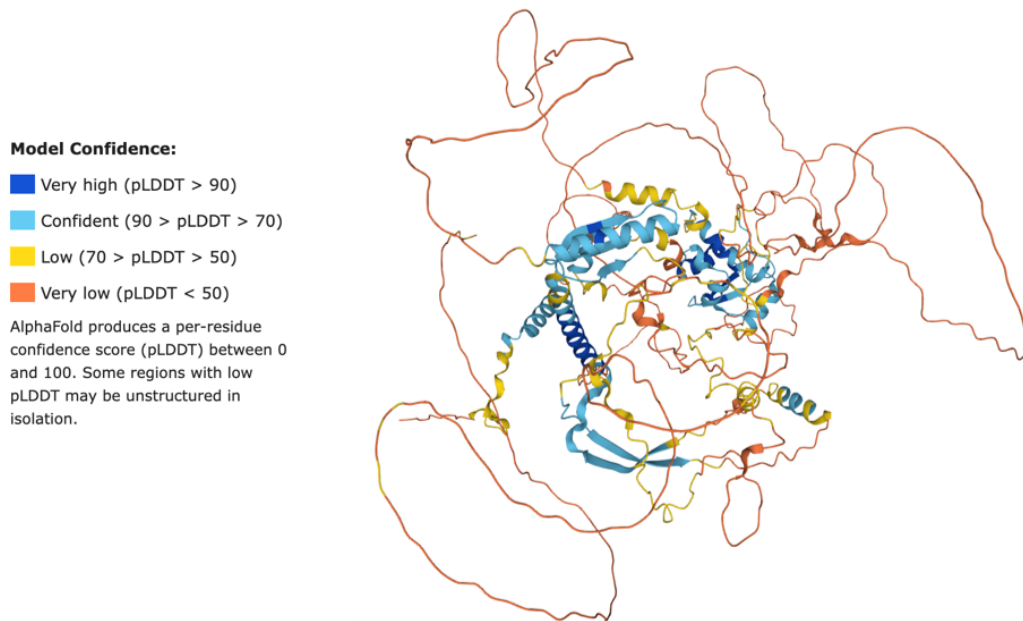
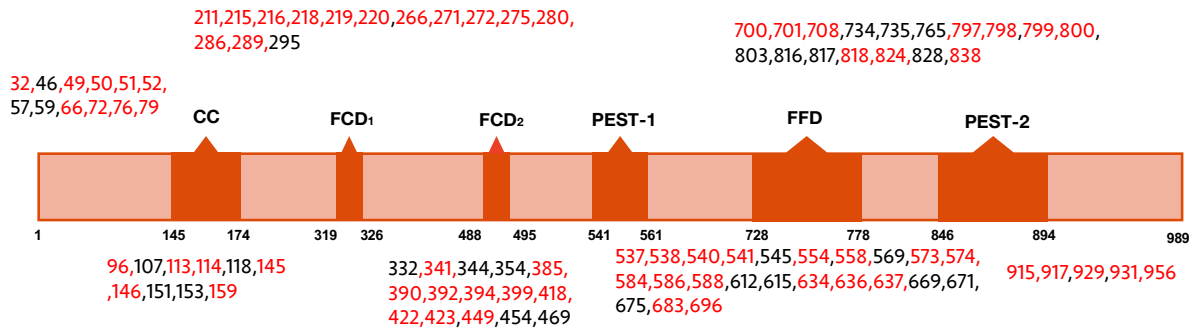| Site	np-FRQ (G)	p-FRQ (G)
NT	1.75	1.87
490C	1.97	2.47
658C	1.97	2.01
746C	1.76	1.82

CT	2.30	1.70

Table S5: R-square values for the quality of the two component gaussian fits to the distance distributions.

|	370	490	658	746
370		0.99, 0.99	0.96, 0.99	NA, 0.99
490			0.94, 0.99	0.99, 0.99
658				0.99, 0.95
746				

Note: There are two values reported in each cell – the first value corresponds to the R-square value for FRQ only distance while the second value is for the same variant in the FFC complex (i.e., when the FRQ is bound to CK1a and FRH).

Figure S5: AlphaFold model of LFRQ colored by pLDDT score. (Image source: https://www.uniprot.org/uniprotkb/P19970/entry#structure)

211,215,216,218,219,220,266,271,272,275,280, 286,289,295

700,701,708,734,735,765,797,798,799,800, 803,816,817,818,824,828,838

32,46,49,50,51,52, 57,59,66,72,76,79

CC   FCD₁   FCD₂   PEST-1   FFD   PEST-2

1   145   174   319   326   488   495   541   561   728   778   846   894   989

96,107,113,114,118,145 ,146,151,153,159

332,341,344,354,385, 390,392,394,399,418, 422,423,449,454,469

537,538,540,541,545,554,558,569,573,574, 584,586,588,612,615,634,636,637,669,671, 675,683,696

915,917,929,931,956

Figure S2: Domain map of FRQ with phospho-sites (as identified by mass-spec) highlighted. The sites in red were also identified in (21, 22).

p-FRQ
np-FRQ
p-FFC
np-FFC
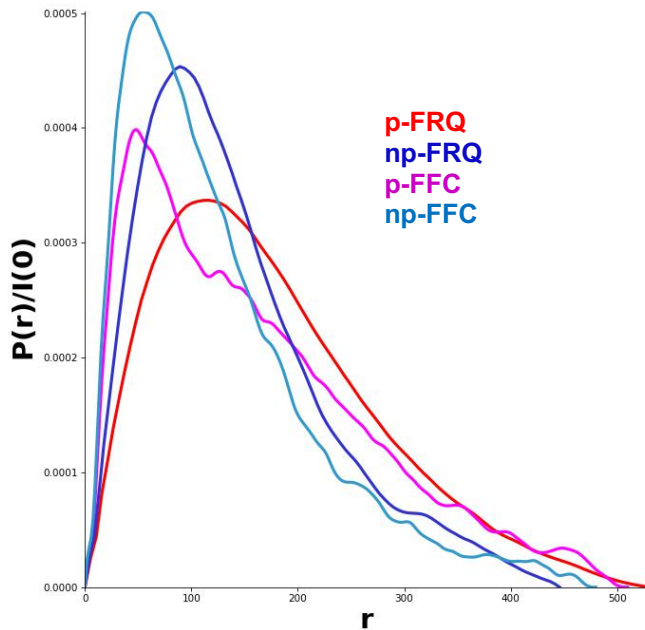
Figure S3: Pair-wise distance distributions calculated from SAXS data for p-FRQ (red), np-FRQ (dark blue), p-FFC (magenta), and np-FFC (light blue).

40
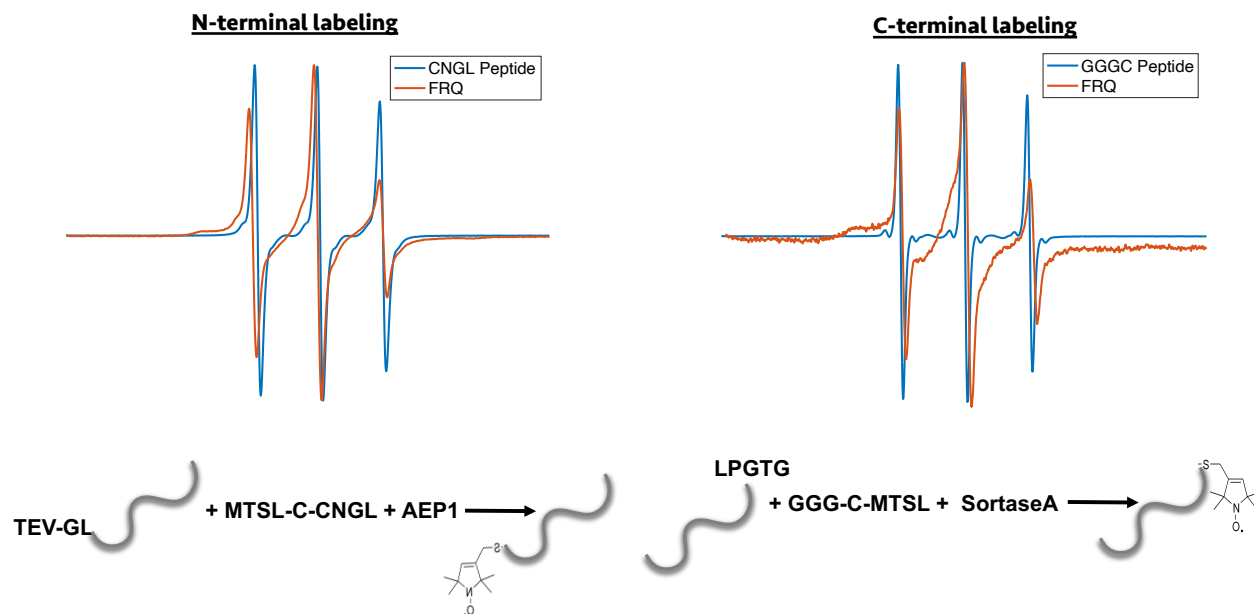
Figure S4: Enzymatic labeling of FRQ at its termini. X-band (9.8 GHz) RT cw-ESR measurements for the spin-labeled peptide by itself and when it has been grafted onto either the N or C-terminus of FRQ.
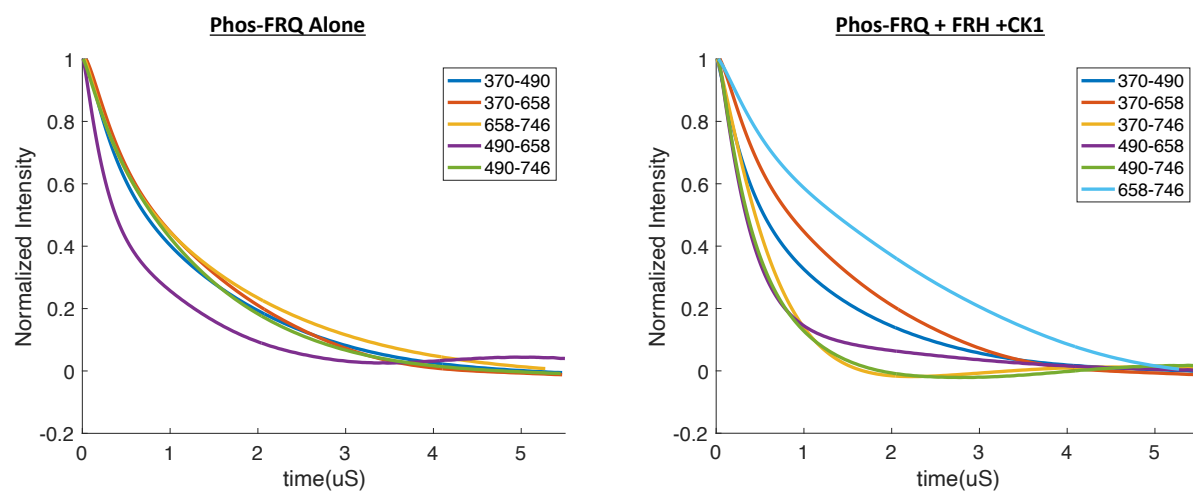
Figure S5: Baseline-corrected time domain fit traces from Q-band DEER experiments of different double-cysteine FRQ mutants alone (left) and within the FFC (right). Data was denoised by WavPDS; original data are are shown in Supplementary Figures S5 and S6.
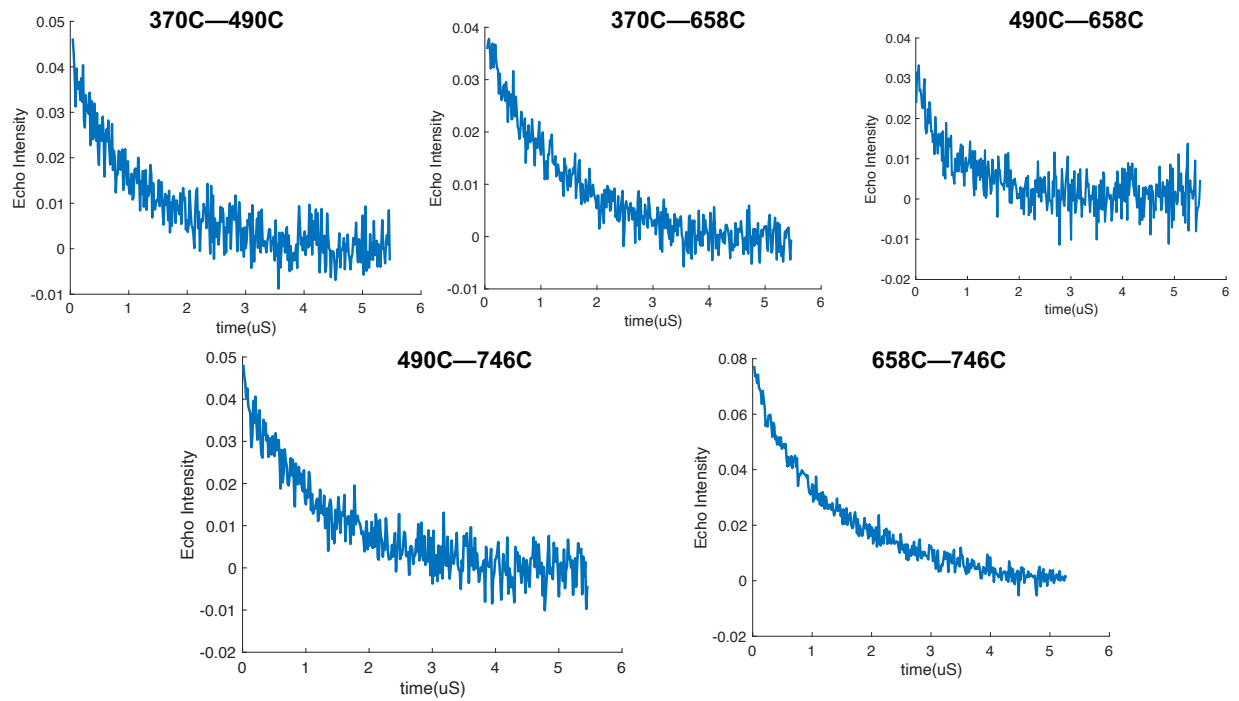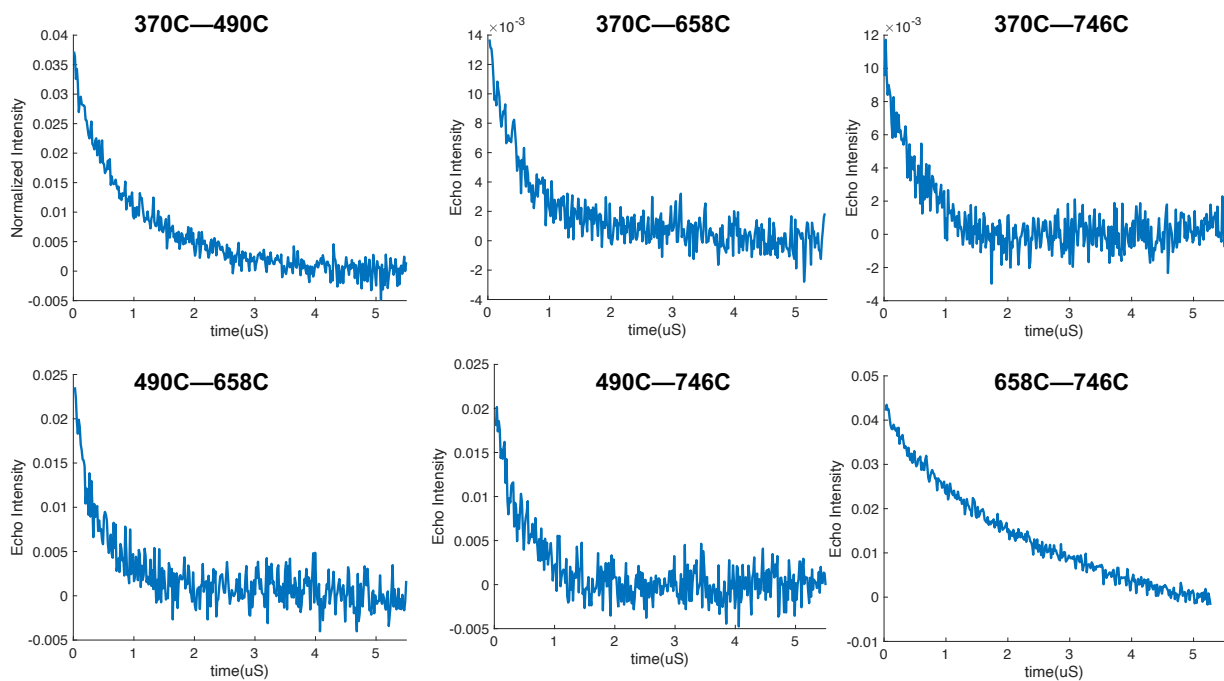
Figure S6: Raw time domain traces from DEER experiments of different double-cysteine FRQ variants. The spins were present on the residue number of FRQ that is highlighted for example '370-490' refers to FRQ spin-labeled at the 370C and 490C site and the DEER experiment probed the dipolar coupling of the spins at these sites.
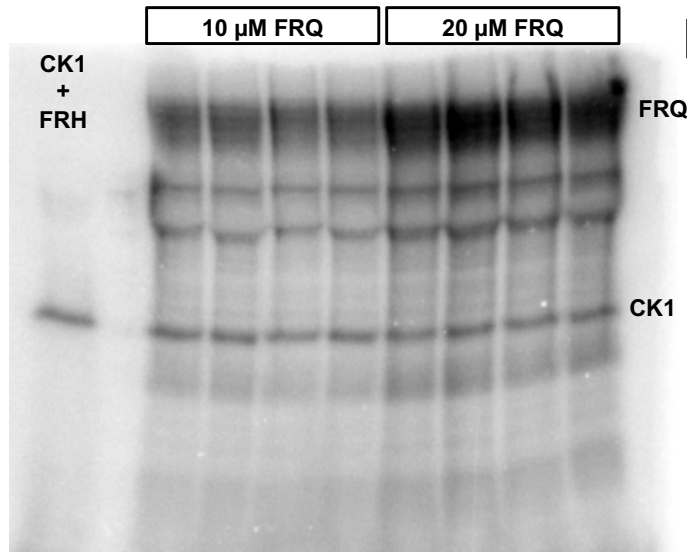
**Figure S7**: Full autoradiograph of np-FRQ phosphorylation by CK1 and γ-^{32}P-ATP from Figure 4A inset.
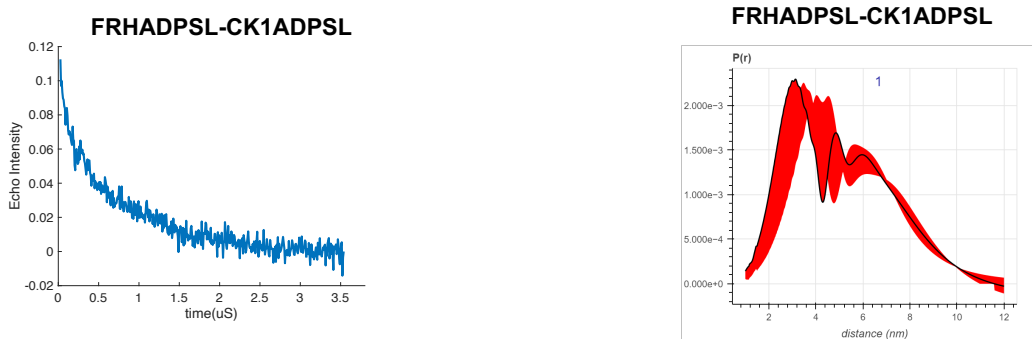
Figure S8: Raw time domain traces and error analyses from DEER experiments targeting the ATP-binding pockets of FRH and CK1. The DEER experiment probed the dipolar coupling of the spins in the ADP-β-S-SL molecule that was present in ATP-binding pocket of FRH or CK1.


Figure S9: Raw time domain traces from DEER experiments of different double-cysteine FRQ variants within the FFC (i.e., when FRQ was bound to FRH and CK1a). The spins were present on the amino acid number of FRQ that is highlighted for example '370-490' refers to FRQ spin-labeled at the 370C and 490C site and the DEER experiment probed the dipolar coupling of the spins at these sites.
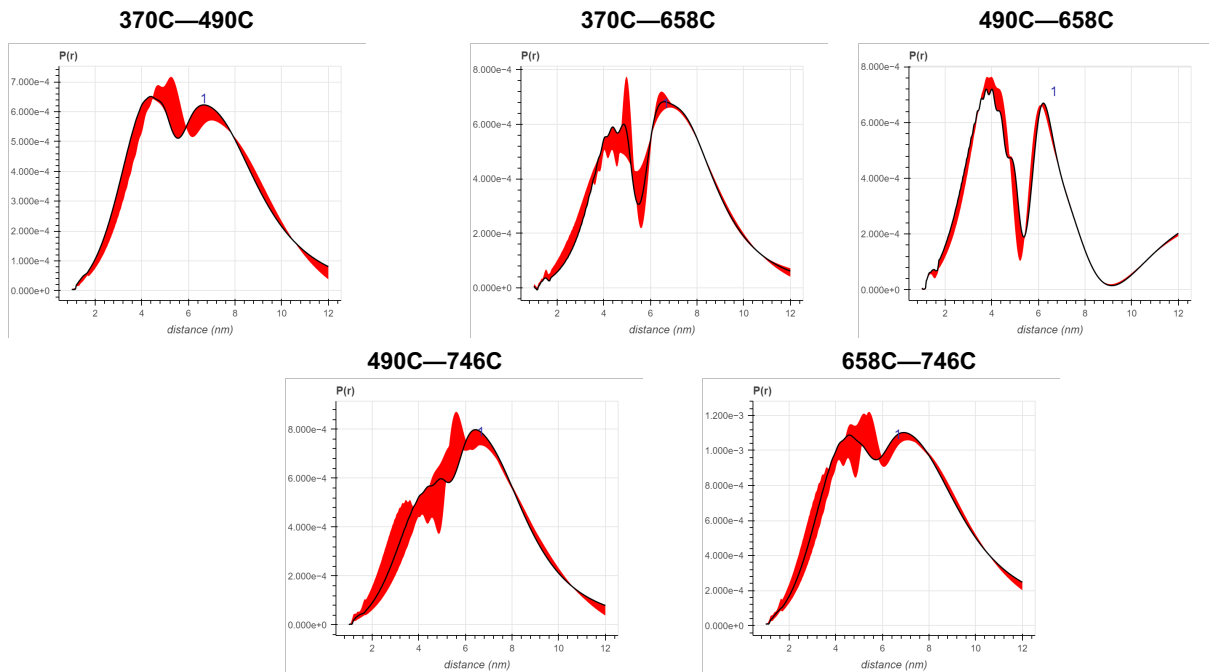
Figure S10: Error analysis of the distance distributions produced from DEER experiments of different double-cysteine FRQ variants. The spins were present on the amino acid number of FRQ that is highlighted for example '370-490' refers to FRQ spin-labeled at the 370C and 490C site and the DEER experiment probed the dipolar coupling of the spins at these sites.
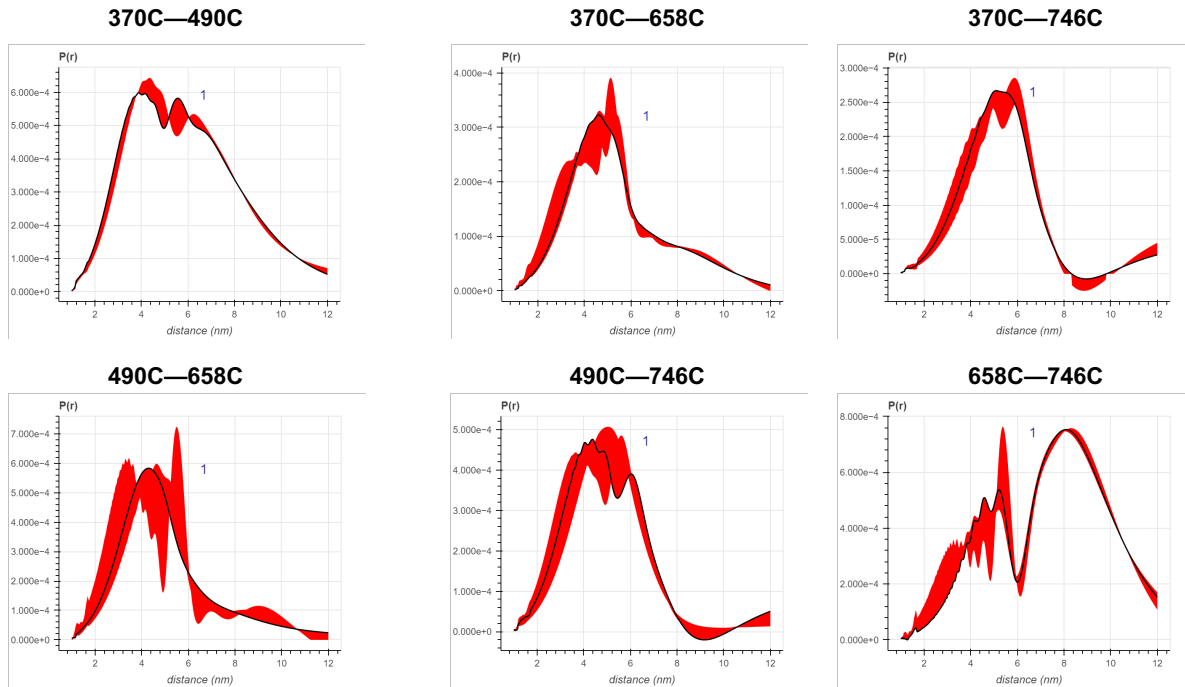
Figure S11: Error analysis of the distance distributions produced from DEER experiments of different double-cysteine FRQ variants within the FFC (i.e., when FRQ was bound to FRH and CK1). The spins were present on the amino acid number of FRQ that is highlighted for example '370-490' refers to FRQ spin-labeled at the 370C and 490C site and the DEER experiment probed the dipolar coupling of the spins at these sites.
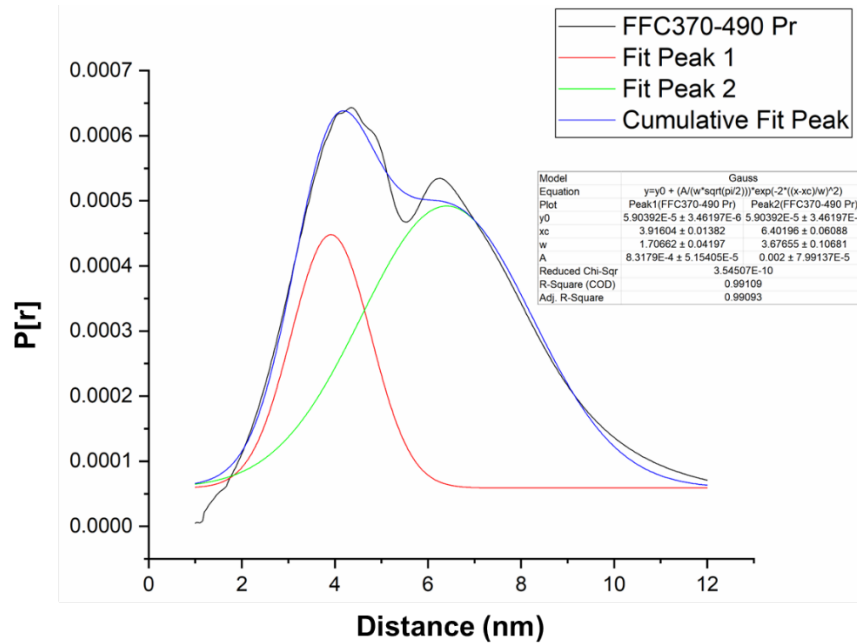
Figure S12: The two component Gaussian fitting of the distance distribution (P[r]) obtained from SVD for FFC 370-490 (i.e., spins were placed on resides 370 and 490 on FRQ, and this protein was bound to CK1 and FRH). No constraints were placed on the width, position, or amplitude of either component and the best fit values were obtained by minimizing the difference between the fits and the SVD distance distributions. Similar fits were carried out for all the different variants. The quality of the fit is reported by the R-square values and ranged between 0.94-0.99 for all the samples tested. They are reported in Table S5.
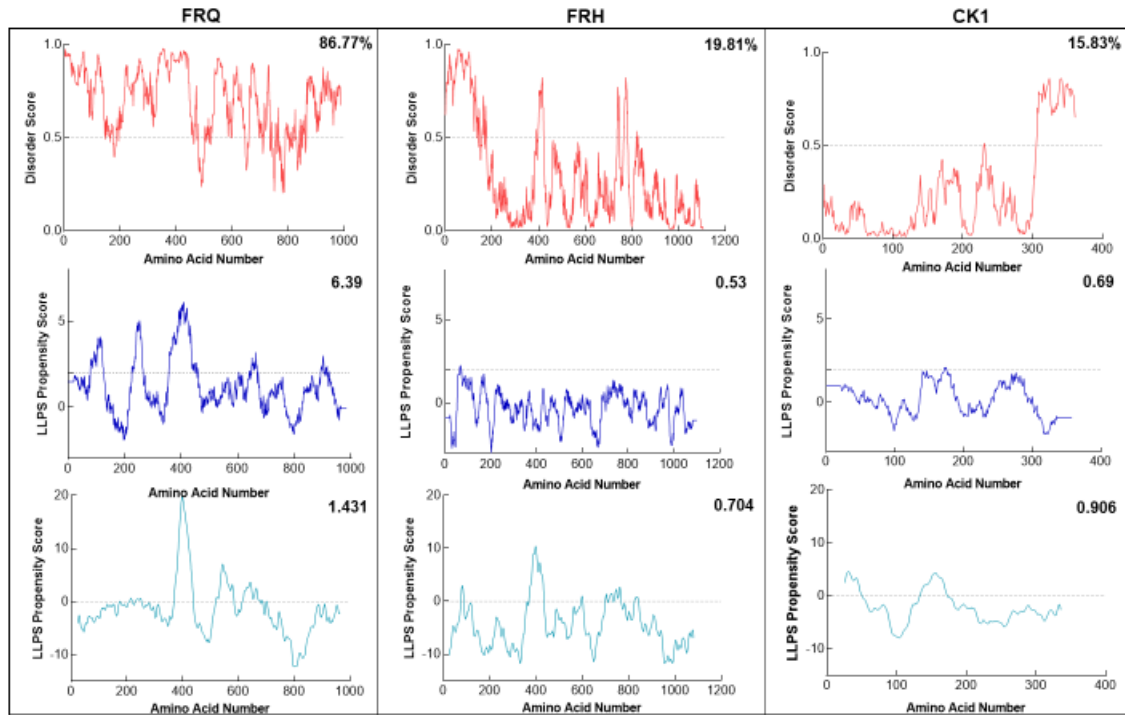
Figure S13: FRQ, but not FRH or CK1, is highly disordered and predicted to undergo LLPS. Shown are the disorder and LLPS propensity scores of the members for the FFC complex, FRQ, FRH and CK1. Columns from left to right are disorder and phase separation predictions for FRQ, FRH and CK1, respectively. Disorder graphs (red) were computed using the IUPred2A program (10) where values above a 0.5 threshold (dashed line) are considered disordered. LLPS propensity predictions were computed using the "Pi-Pi" (blue) (13) and catGRANULE (light blue) (14). Shown on the top right corner of each graph are the percent disorder or LLPS propensity scores of each protein.
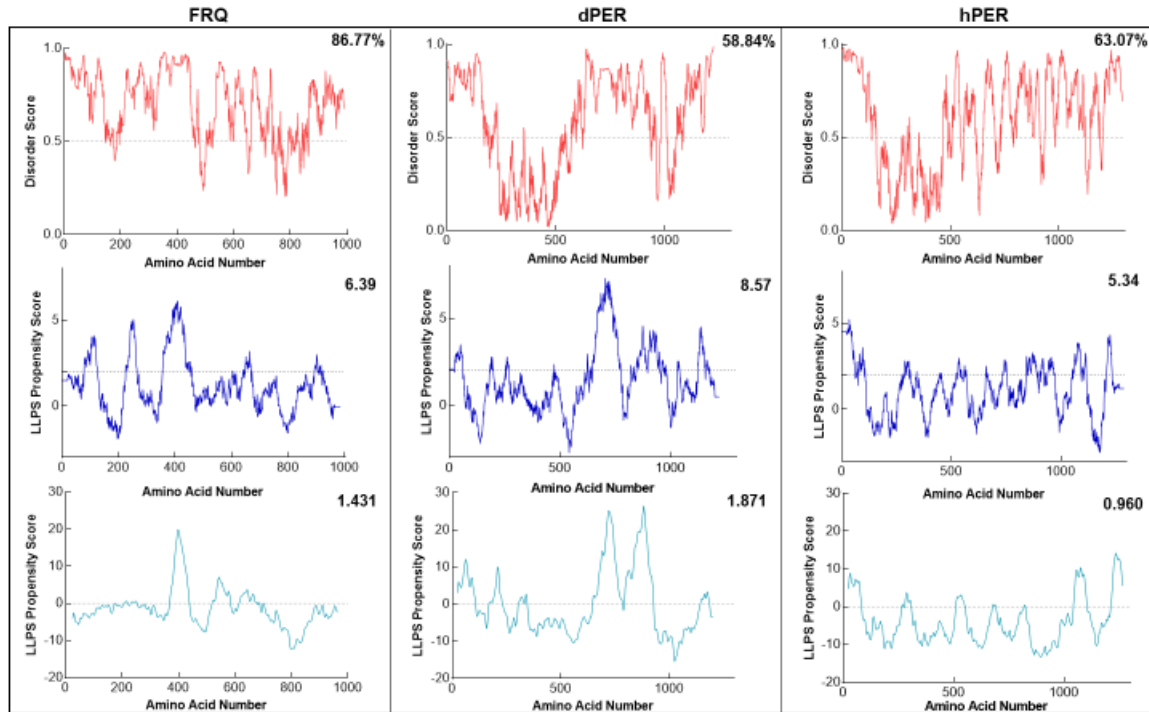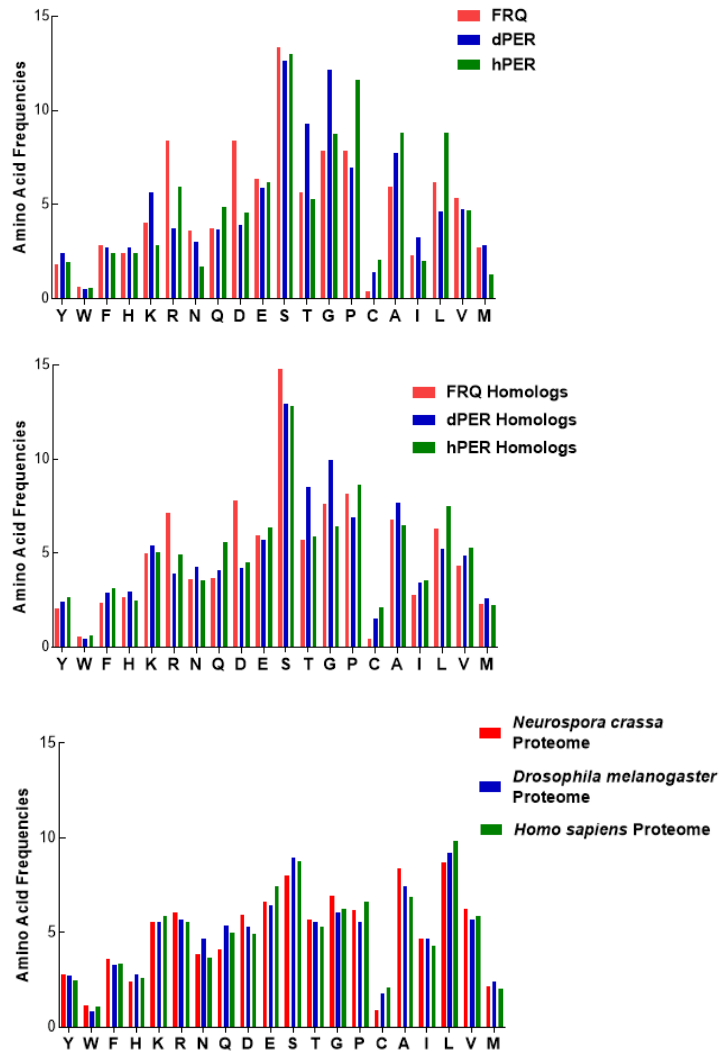
Figure S14: FRQ and its functional homologs are predicted to undergo LLPS. Shown are the disorder and LLPS propensity scores for FRQ, dPER1 and hPER1. Data for the disorder graphs (red) were computed using the IUPred2A program where values above a 0.5 threshold (dashed line) are considered disordered. Pi-pi predictions (blue) were computed using (13), while catGranule predictions (light blue) were computed using catGranule server (14). Shown on the top-right corner of each graph are the percent disorder, PScore or catGranule score for each protein. FRQ, dPER1 and hPER1 are all predicted to be highly disordered (86.77%, 58.84% and 63.07%, respectively) and undergo LLPS.
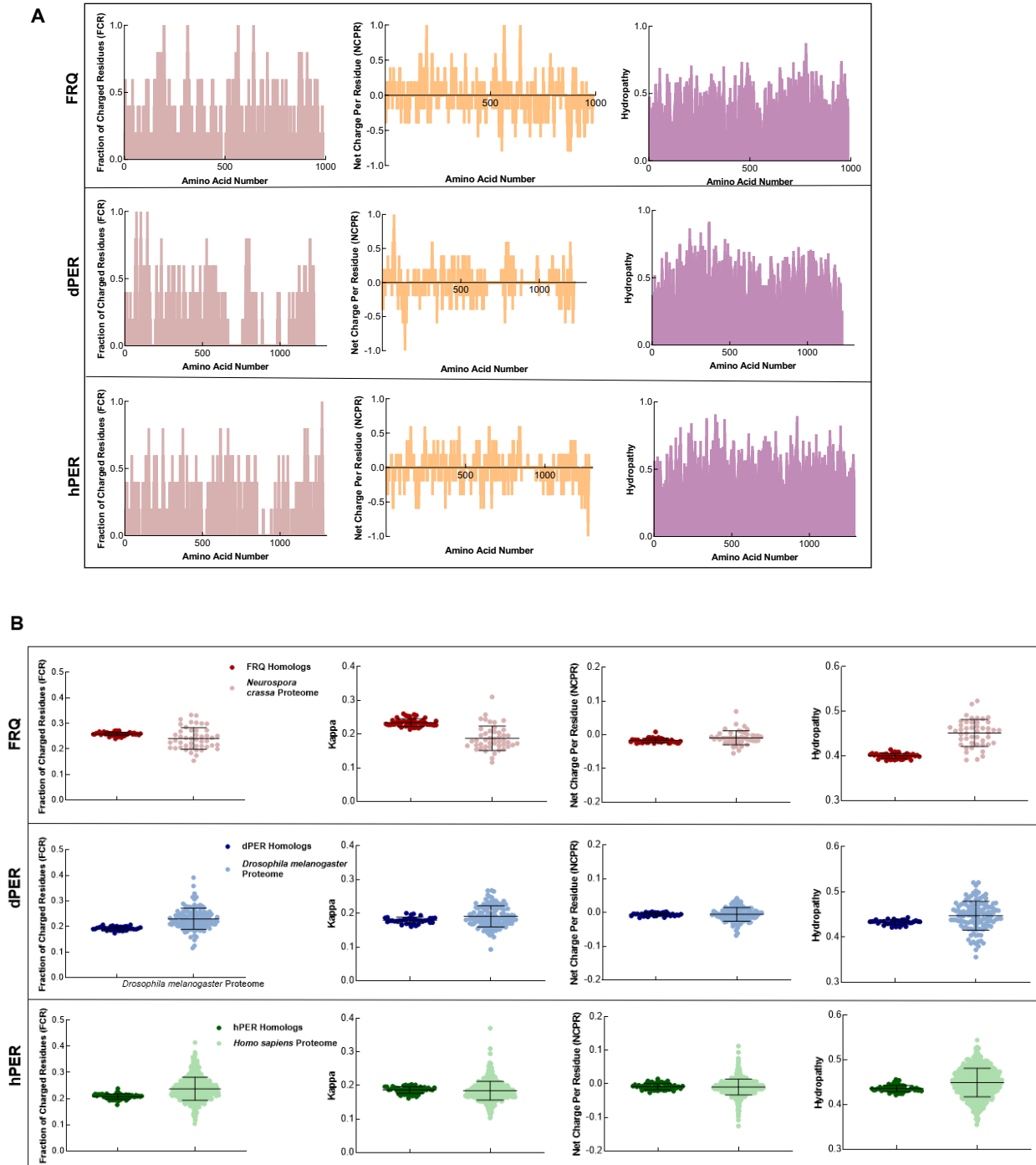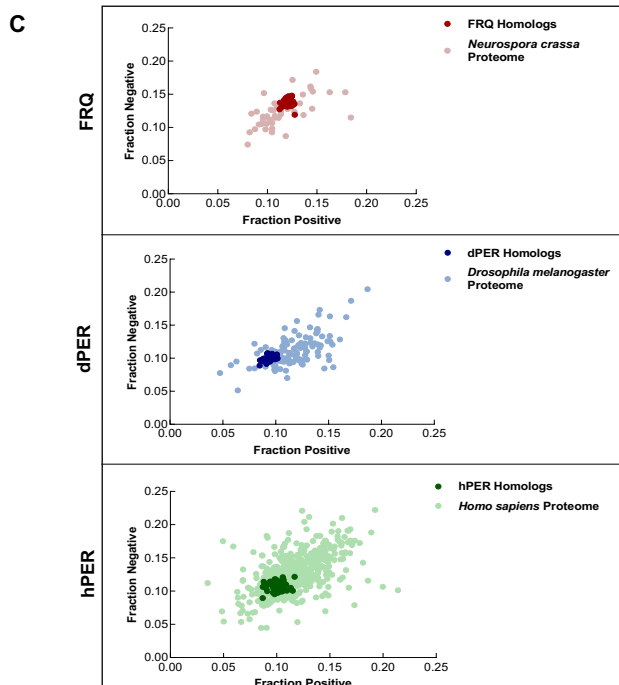
Figure S15: FRQ and its homologs, dPER1 and hPER1, have similarly disparate physicochemical properties compared to their proteomes. (A) Shown are the distribution of fraction of charged residues (FCR), net charge per residue (NCPR), and hydropathy along the sequence of FRQ, dPER1 and hPER1. (B) Sequence characteristics of FRQ and its homologs, dPER1 and hPER1. Various protein sequence parameters are calculated using localCIDER (9) and displayed including fraction of charged residues (FCR), the degree of charge mixing (Kappa), net charge per residue (NCPR), and hydropathy (the hydrophobic and hydrophilic character of protein chain as defined by (23)) for the UniProtRef50 clusters of FRQ (red), dPER1(blue) and hPER1 (green). For comparison are shown protein sequences of similar length from the SWISS-Prot reviewed proteomes of *Neurospora crassa* (pink), *Drosophila melanogaster* (light blue) and *Homo sapiens* (light green). Hydropathy is consistently low for the clock proteins and FRQ orthologs have a high degree of charge separation, i.e. tracks of negative and positive residues (high kappa). High kappa values are common for proteins that phase separate (24). (C) Classification of the charge properties of the Ref50 clusters of FRQ and its functional homologs, dPER1 and hPER1. Das-Pappu phase plots showing the fraction of negatively vs positively charge residues for the UniProtRef50 clusters of FRQ (red), Neurospora crassa proteome control (pink), dPER1 (blue), *Drosophila melanogaster* proteome control (light blue), hPER1 (green) and Homo sapiens proteome control (light green). Shown are the fraction of negative residues versus fraction of positive residues for each cluster of homologs and their controls (similar size proteins from their respective proteomes). Despite the lack of amino acid conservation between the functional homologs of FRQ, dPER1 and hPER1, the ratio of fraction negative to fraction positive residues are similar among the clock proteins. dPER and hPER1 have a similarly low value of both fraction positive and fraction negative compared to their respective proteomes, whereas the fraction positive and fraction negative residues are both higher in FRQ. Note: Ref50 is a clustering method utilized by uniport and is defined in (25).

Figure S16: **FRQ and its functional homologs dPER1 and hPER1 have similar amino acid composition compared to their respective proteomes.** FRQ and its functional homologs dPER1 and hPER1 have similar amino acid compositions, which differs substantially from that of their respective proteomes. The amino acid composition for FRQ, dPER1 and hPER1 and their respective homolog clusters and proteomes are shown. Generally, G, S, T and P residues are enriched whereas hydrophobic (A, I, L, V) residues are relatively depleted for FRQ, dPER1, hPER1 and their homologs compared to their proteomes. Unlike dPER1 and hPER1 and their homologs, FRQ and its homologs are also highly enriched in R and D.
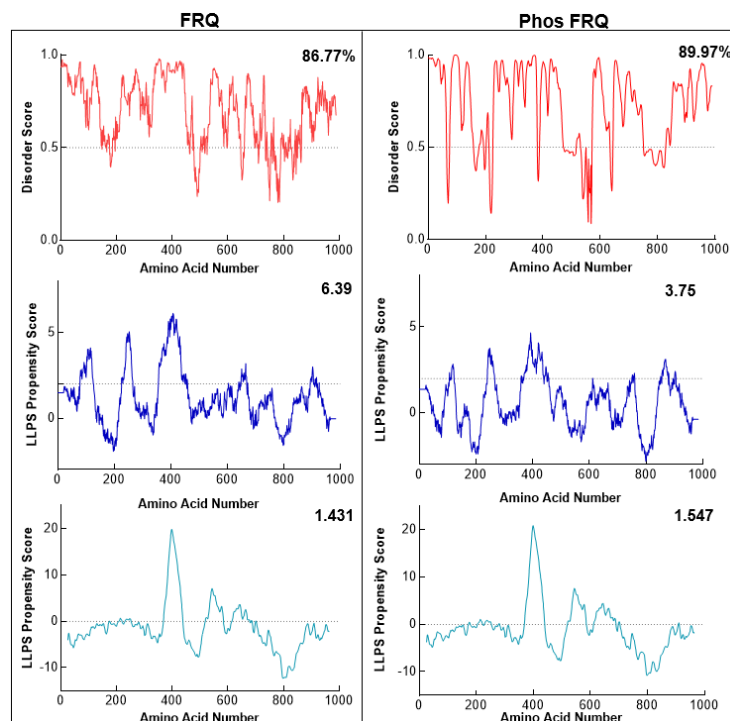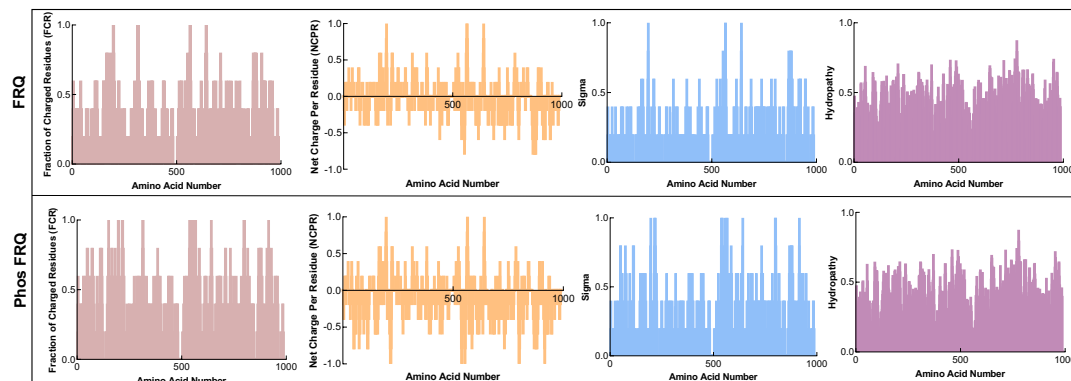
Figure S17: Phosphorylation modulates the physicochemical properties of FRQ. Shown are the distribution of fraction of charged residues (FCR), net charge per residue (NCPR), and hydropathy along the sequence of np and p-FRQ (top panel). In the bottom panel, shown are the disorder and LLPS propensity scores for np and p-FRQ. Data for the disorder graphs (red) were computed using the IUPred2A program (10) where values above a 0.5 threshold (dashed line) are considered disordered. Pi-pi predictions (blue) were computed using, while catGranule predictions (light blue) were computed using catGranule server (14). Shown on the top-right corner of each graph are the percent disorder, PScore or catGranule score for each protein. Note: Glu(E) residues were employed as phospho-mimetics in all analysis.
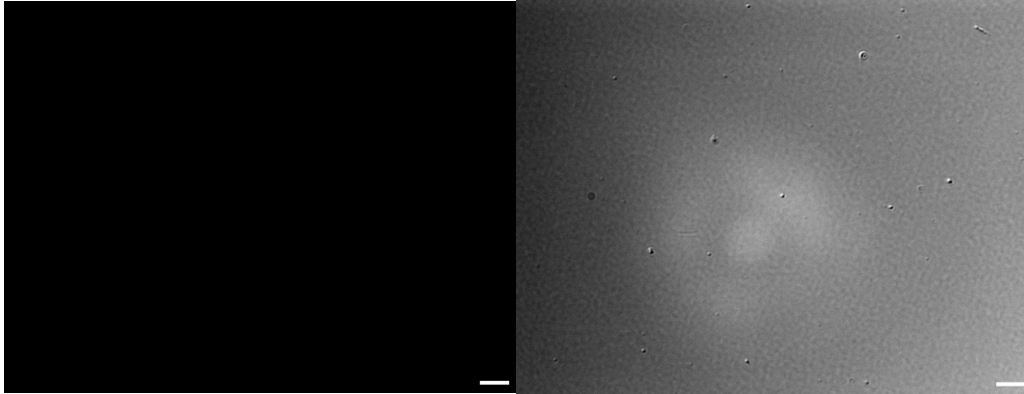
Figure S18: Fluorescence (left) and DIC (right) microscopy images at RT of phase-separated non-phosphorylated FRQ droplets with cy5-labeled CheY visualized using cy-5 fluorescence. Scale bar = 5 microns. Cy5-labeled CheY does not localize to the droplets.
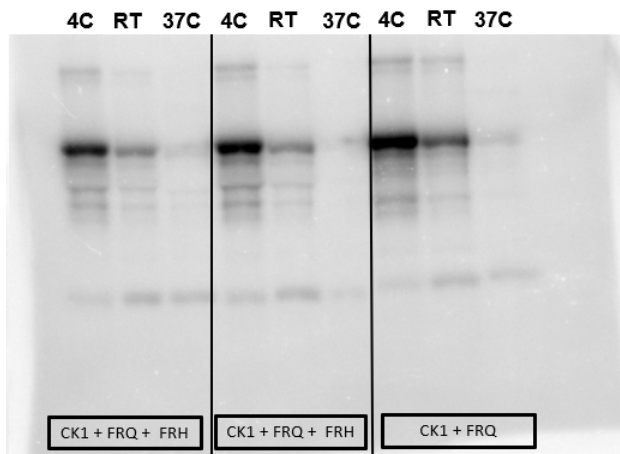
Figure S19: Full radiograph of np-FRQ phosphorylation by CK1 and γ-^{32}P-ATP from Figure 7.

References:

1. C. Querfurth *et al.*, Posttranslational regulation of Neurospora circadian clock by CK1a-dependent phosphorylation. *Cold Spring Harbor symposia on quantitative biology* **72**, 177-183 (2007).

2. J. B. Hopkins, R. E. Gillilan, S. Skou, BioXTAS RAW: Improvements to a free open-source program for small-angle X-ray scattering data reduction and analysis. *Journal of Applied Crystallography* **50**, 1545-1553 (2017).

3. S. Chandrasekaran *et al.*, Tuning flavin environment to detect and control light-induced conformational switching in Drosophila cryptochrome. *Communications Biology 2021 4:1* **4**, 1-12 (2021).

4. G. K. T. Nguyen, Y. Cao, W. Wang, C. F. Liu, J. P. Tam, Site-Specific N-Terminal Labeling of Peptides and Proteins using Butelase 1 and Thiodepsipeptide. *Angewandte Chemie-International Edition* **54**, 15694-15698 (2015).

5. A. R. Muok, T. K. Chua, H. Le, B. R. Crane, Nucleotide Spin Labeling for ESR Spectroscopy of ATP-Binding Proteins. *Applied Magnetic Resonance* **49**, 1385-1395 (2018).

6. M. Srivastava, J. H. Freed, Singular Value Decomposition Method to Determine Distance Distributions in Pulsed Dipolar Electron Spin Resonance. *Journal of Physical Chemistry Letters* **8**, 5648-5655 (2017).

7. M. Srivastava, E. R. Georgieva, J. H. Freed, A New Wavelet Denoising Method for Experimental Time-Domain Signals: Pulsed Dipolar Electron Spin Resonance. *Journal of Physical Chemistry A* **121**, 2452-2465 (2017).

8. A. Bateman *et al.*, UniProt: the universal protein knowledgebase in 2021. *Nucleic Acids Research* **49**, D480-D489 (2021).

9. A. S. Holehouse, R. K. Das, J. N. Ahad, M. O. G. Richardson, R. V. Pappu, CIDER: Resources to Analyze Sequence-Ensemble Relationships of Intrinsically Disordered Proteins. *Biophysical Journal* **112**, 16-21 (2017).

10. B. Mészáros, G. Erdös, Z. Dosztányi, IUPred2A: context-dependent prediction of protein disorder as a function of redox state and protein binding. *Nucleic Acids Research* **46**, W329-W337 (2018).

11. V. Muñoz, L. Serrano, Elucidating the folding problem of helical peptides using empirical parameters. *Nature Structural Biology* **1**, 399-409 (1994).

12. J. Jumper *et al.*, Highly accurate protein structure prediction with AlphaFold. *Nature 2021 596:7873* **596**, 583-589 (2021).

13. R. M. Vernon *et al.*, Pi-Pi contacts are an overlooked protein feature relevant to phase separation. *Elife* **7**, e31486 (2018).

14. B. Bolognesi *et al.*, A Concentration-Dependent Liquid Phase Separation Can Cause Toxicity upon Increased Protein Expression. *CellReports* **16**, 1-10 (2016).

15. B. M. Bartholomai (2022) Cell biological dissection of the Neurospora circadian oscillator: Tools, approaches and fundamental observations. in *Biochemistry and Genetics* (Dartmouth College, Hanover, NH).

16. H. J. Vogel, A convenient growth medium for Neurospora (Medium N). *Microb. Genet. Bull.* **13**, 42-43 (1956).

17.   J. Schindelin *et al.*, Fiji: an open-source platform for biological-image analysis. *Nature Methods* **9**, 676-682 (2012).

18.   C. Querfurth *et al.*, Circadian Conformational Change of the Neurospora Clock Protein FREQUENCY Triggered by Clustered Hyperphosphorylation of a Basic Domain. *Molecular Cell* **43**, 713-722 (2011).

19.   P. Cheng, Q. He, Q. He, L. Wang, Y. Liu, Regulation of the Neurospora circadian clock by an RNA helicase. *Genes and Development* **19**, 234-241 (2005).

20.   J. Guo, P. Cheng, Y. Liu, Functional significance of FRH in regulating the phosphorylation and stability of Neurospora circadian clock protein FRQ. *J. Biol. Chem.* **285**, 11508-11515 (2010).

21.   C. L. Baker, A. N. Kettenbach, J. J. Loros, S. A. Gerber, J. C. Dunlap, Quantitative Proteomics Reveals a Dynamic Interactome and Phase-Specific Phosphorylation in the Neurospora Circadian Clock. *Molecular Cell* **34**, 354-363 (2009).

22.   C. T. Tang *et al.*, Setting the pace of the Neurospora circadian clock by multiple independent FRQ phosphorylation events. *Proc. Natl. Acad. Sci. USA* **106**, 10722-10727 (2009).

23.   J. Kyte, R. F. Doolittle, A simple method for displaying the hydropathic character of a protein. *Journal of Molecular Biology* **157**, 105-132 (1982).

24.   R. Somjee, D. M. Mitrea, R. W. Kriwacki (2020) Exploring Relationships between the Density of Charged Tracts within Disordered Regions and Phase Separation. in *Pacific Symposium on Biocomputing* (Hi), pp 207-218.

25.   M. Steinegger, J. Söding, Clustering huge protein sequence sets in linear time. *Nature Communications* **9**, 2542 (2018).